SAPPHIRE BENEATH THE RICH BLACK SOIL OF MULING, NORTHEASTERN CHINA

Yimiao Liu and Ren Lu

The rich black soil of Muling in northeastern China yields not only abundant crops but also glittering gem corundum. In this study, gemological quality and characteristics and provenance-related features of sapphire from Muling are first reported with comprehensive analytical results. Muling sapphire exhibits a wide spectrum of hue and saturation. Mineral inclusions (e.g., rutile, zircon, anorthite, and pyrope) as well as other distinctive internal features (e.g., polysynthetic twinning accompanied by intersecting tubes, iridescent hexagonal thin films, and angular color zoning) are identified by microscopic observation and Raman spectroscopy. Spectral features and trace element chemistry of the various colors of gem-quality Muling sapphire are analyzed by ultraviolet/visible/near-infrared spectroscopy and laser ablation–inductively coupled plasma–mass spectrometry. To assess the characteristics of Muling sapphire against well-known corundum sources worldwide, inclusion analysis and trace element discrimination diagrams are utilized. Analytical results indicate that Muling sapphire originated from a more diverse geological environment than typical magmatic or metamorphic origin. The Muling deposit shows great potential to produce fine gem-quality sapphire material.

China has become a strong force in both production and consumption of gems and jewelry in the past two decades, and it is the fastest-growing consumer market for fine gemstones. Chinese consumers have led the positive growth trend in the global luxury market and are on track to claim the largest share of the market by 2025, according to a Bain & Company study (Lannes and Zhang, 2020). Awareness of colored stones—particularly the classic "big three" of ruby, sapphire, and emerald—has reached unprecedented heights in China in less than a decade.

Despite its diverse geographic and geological landscapes, China has not been known historically as a producer of fine-quality gems such as ruby and sapphire. The only source of Chinese sapphire known to much of the world is Shandong, where large and clean but oversaturated blue sapphire is mined. During the 1980s and 1990s, other Chinese sources were also reported, mostly domestically, including Penglai in Hainan Island and Mingxi in Fujian Province (all along the east coast of China) and described as classic magmatic sapphire deposits (Keller and Keller, 1986; Keller and Wang, 1986; Wang, 1988; Guo et al., 1992). Attempts to lighten the sapphire's color from inky blue to a more marketable color (Wang et al., 1992; Cheng et al., 2009) have been unsuccessful. This Chinese sapphire material was therefore considered of little economic value on the global gem market. The situation is similar with ruby production. Ruby has been reported from the Ailaoshan area in Yunnan Province and the Xinjiang Uyghur Autonomous Region with little specific description of its quality or gemological characteristics (Galibert and Hughes, 1995; J. Zhang et al., 2003; Huang et al., 2021). The perception from such reports is that sapphire and ruby from China is not of fine quality.

The perceived scarcity of domestic gem resources in China motivated the authors to investigate identified corundum deposits for their potential. One is the Muling area, which lies on an exceptionally fertile black soil region (Sorokin et al., 2021). Our research reveals that hidden beneath this rich black soil is an underexplored resource of sapphire (figure 1).

See end of article for About the Authors and Acknowledgments.

GEMS & GEMOLOGY, Vol. 58, No. 3, pp. 290–317,
http://dx.doi.org/10.5741/GEMS.58.3.290

Figure 1. *These Muling sapphires (0.1–8.2 ct) in a variety of shapes and cuts demonstrate the full range of hue, saturation, and clarity coming from this deposit. Photo by Ren Lu.*

Reports about Muling's mineral resources are limited compared with those about other Chinese corundum deposits. Su (1990) first reported sapphire production in this area. Galibert and Hughes (1995) also mentioned the deposit briefly. Jianxun Sun, who worked on a geological survey of Heilongjiang Province, published studies about the geological characteristics of corundum deposits in this region (Sun et al., 2005) and documented the mineralogical features of Muling sapphire from a geological perspective (Sun, 1995). Qiu et al. (2007) investigated the geological background of Muling by analyzing zircon megacrysts. Chen et al. (2011, 2013) studied the gemological features of gem-quality zircon and garnet. However, no publication has drawn conclusions about the quality and the provenance-related characteristics of Muling sapphire.

The present authors began systematic studies of Muling sapphire in 2014 and previously provided a brief introduction in *G&G* (Liu and Lu, 2016). Author RL's research team studied gem-quality megacrysts (garnet, clinopyroxene, and orthopyroxene) hosted by the Cenozoic alkali basalts in the Muling area, providing more information on the parental magmatic systems of this area (Hu et al., 2022). The comprehensive gemological features and

In Brief

- The Muling deposit, in Heilongjiang Province of northeastern China, produces fine sapphire material.
- Muling sapphire exhibits a wide variety of hues and saturations.
- Muling sapphire originated from a more diverse geological environment than typical magmatic or metamorphic origin.

Figure 2. Geographic map of reported corundum occurrences in China. The red marker on the upper right represents the Muling area.

advanced analysis of Muling sapphire, including preliminary data to aid in origin determination, will be presented in this article.

GEOGRAPHY AND HISTORY

Muling, with a population of 320,000, is a very small community by Chinese standards. It lies in eastern Heilongjiang Province, near the Chinese-Russian border (figure 2). The Muling River flows through this mountainous city from north to south. Although small, Muling plays an important role. Located on exceptionally fertile land covered with black soil, the area has been referred to as the country's "grain basket" (Gu et al., 2018) (figure 3). Muling is famous for its richness in natural resources, with a saying of "Two yellow, two black, and one treasure." This refers to golden and yellow sun-cured tobacco ("two yellow"), coal and graphite ("two black"), and gemstones ("one treasure"). With the adjoining city of Suifenhe as one of the largest Sino-Russian centers, all of these products can be shipped across the country by highway. Although the high-latitude cold climate limits human activities, it protects the natural environment and wild animals. Muling is part of the Northeast China Tiger and

Figure 3. A vast expanse of brightly colored marigolds in a field of black soil in the Muling region. The gem-producing region lies in the distance. Photo by Ren Lu.

Figure 4. This photo of the Muling sapphire deposit, taken in April 2018, shows the trommel left unused. In this area, mining operations must cease for more than half the year because of freezing temperatures. The authors visited the mining site in June 2018, when weather conditions permitted mining activities. Photo by Aijun Yi.

Leopard National Park. These precious animals are listed on the International Union for Conservation of Nature (IUCN) Red List of Threatened Species (Miquelle et al., 2011), and their populations are even rarer than that of the giant panda. A rugged, warm, and generous character defines the people who live here.

The name *Muling* is a transliteration of a Manchurian word to contemporary Mandarin Chinese that means "horse breeding farm." According to local annals (Editorial Committee of Muling, 1989), it was reserved as a "royal forbidden area" and served as a horse range for the royal army in the Qing Dynasty (1636–1912 CE). This pristine region was untouched until World War II. After the establishment of the People's Republic of China in 1949, new geological surveys targeting strategic ore deposits began throughout the country. Potential gem resources in the Muling area were originally recorded in these geological reconnaissance surveys. But it was not until the late 1980s that the public took notice. A series of studies were conducted by the Geological Survey of Heilongjiang Province to search for gem resources.

Starting in the late 1990s, Muling attracted the attention of gem traders from Thailand, who forged an agreement with the local government and brought in mining machinery. One of the machines was left in Muling and is still fully functional today (figure 4). Aijun Yi, former director of the mineral resource administration in Muling, participated in cooperative exploitation. This cooperation continued until 2002, and he recalled that the total production of corundum during official mining activities from the late 1990s to 2002 was 10,000 carats (Yi A., pers. comm., 2018). After that, commercial mining activities ceased until small-scale mining was carried out by a domestic mining company for a few months in 2017. Due to the policy of prime farmland preservation, however, there is no mining in Muling as of the time of this writing. Local farmers usually collected gemstones such as corundum, garnet, and feldspar from the low-lying area downstream from the mountains, which is said to abound with precious stones.

Figure 5. Author YL sits on one of the local basalt columns measuring over 50 cm in diameter. Photo by Ren Lu.

GEOLOGICAL SETTING

Northeastern China belongs to the eastern segment of the Central Asian Orogenic Belt, which lies between the North China Craton and the Siberian Craton (Wilhem et al., 2012). This area underwent the tectonic evolution of the amalgamation during the Paleozoic (Wang et al., 2019), overprinted by circum-Pacific tectonic events since the early Mesozoic (Feng et al., 2019; Li et al., 2020), and then entered a phase of the extensive eruption of Cenozoic basalts (Pan et al., 2015). The Muling area lies at the northern section of the Dunhua-Mishan fault, a large thrust fault trending N50°E (Wang and Dou, 1997). The Dunhua-Mishan fault is a branch of the northern part of the N-S trending Tan-Lu fault (Wang et al., 2001; Y.Q. Zhang et al., 2003; Ling et al., 2017), cutting through the Shenyang, Dunhua, and Mishan areas and extending into Russia (Ling et al., 2017). The Tan-Lu fault is a classic example of lithospheric extension between the Xingmeng Orogenic Belt and the Pacific subduction zone (Qiu et al., 2007; Ling et al., 2017).

The corundum-related rocks in the Muling area belong to Tertiary basalts, including dense massive olivine basalt, basaltic pumice, amygdaloidal basalt, and taxitic basalt (figure 5; Sun et al., 2005). Dayan Ridge was the main mining site operated by miners from Thailand, producing large amounts of sapphire of almost all colors as well as a small quantity of ruby material. Another mine is found in the small village of Guangming. Villagers can occasionally find high-quality rough (mainly ruby). Other places such as Li Mountain, Gangouzi, and Hanconggou are also accessible for villagers to collect rough gems (figure 6). These occurrences are all secondary deposits derived from basalts, which are regarded as the gem carrier (Sun, 1995). During the weathering process, heavy minerals are concentrated, including corundum, zircon, spinel, magnetite, ilmenite, augite, garnet (almandine, pyrope), and hematite.

MATERIALS AND METHODS

Samples. For this study, a few thousand pieces of rough corundum were gathered during and after the authors' three field trips to Muling between 2014 and 2018. More than 70% of these samples were donated by Mr. Yi, a lifelong resident who surveyed the Muling region throughout his career. The authors found 20% of the stones from the remnants of the Dayan Ridge deposit mined in the 1990s. Around 5% of the samples with high gem quality were purchased from local farmers through Mr. Yi, especially red samples (again, see figure 1).

From our few thousand pieces of rough, 1,030 were grouped according to color (see figures 7 and 8). Of these, 311 polished samples were used for more detailed studies. The 311 stones were grouped according to color: the red group ("R," including all samples with a dominant red hue—including pink, orangy pink, purple, and purplish red), the light blue group ("LB"), the deep blue group ("DB"), the yellow group ("Y"), and the green group ("G").

The subsequent naming convention for samples is color coded (e.g., DB2 for deep blue sample no. 2). Near-colorless sapphires are not discussed in this paper. The analysis and discussion of low-saturation materials, including near-colorless sapphires, will be presented in a separate study.

After visually and microscopically examining all samples, 311 stones with suitable size (0.5–3.0 ct) were selected, covering a full range of color and not affected by open fissures. Of those, 115 were faceted and 196 were doubly polished into wafers for detailed gemological observation and spectroscopic analysis. In addition, 77 samples were analyzed for trace element compositions. These samples were chosen from polished samples of each color group with variations in hue and saturation. Sample numbers of both faceted and wafer sets can be seen in table 1. Among all wafers, only those with desirable optical homogeneity underwent a complete set of spectroscopic and *in situ* trace element chemical analysis. Most of the visually transparent and homogeneous crystals were further found to exhibit various levels of twinning structures when illuminated under cross-polarized light. Wafers that were optically near perfect or only contained minor optical imperfections were also analyzed for a relatively complete set of spectroscopic characterizations of each color group of samples.

Figure 6. Geological map of corundum deposits in Muling, captured from a 1:200,000 geological map. Modified after Sun (1995).

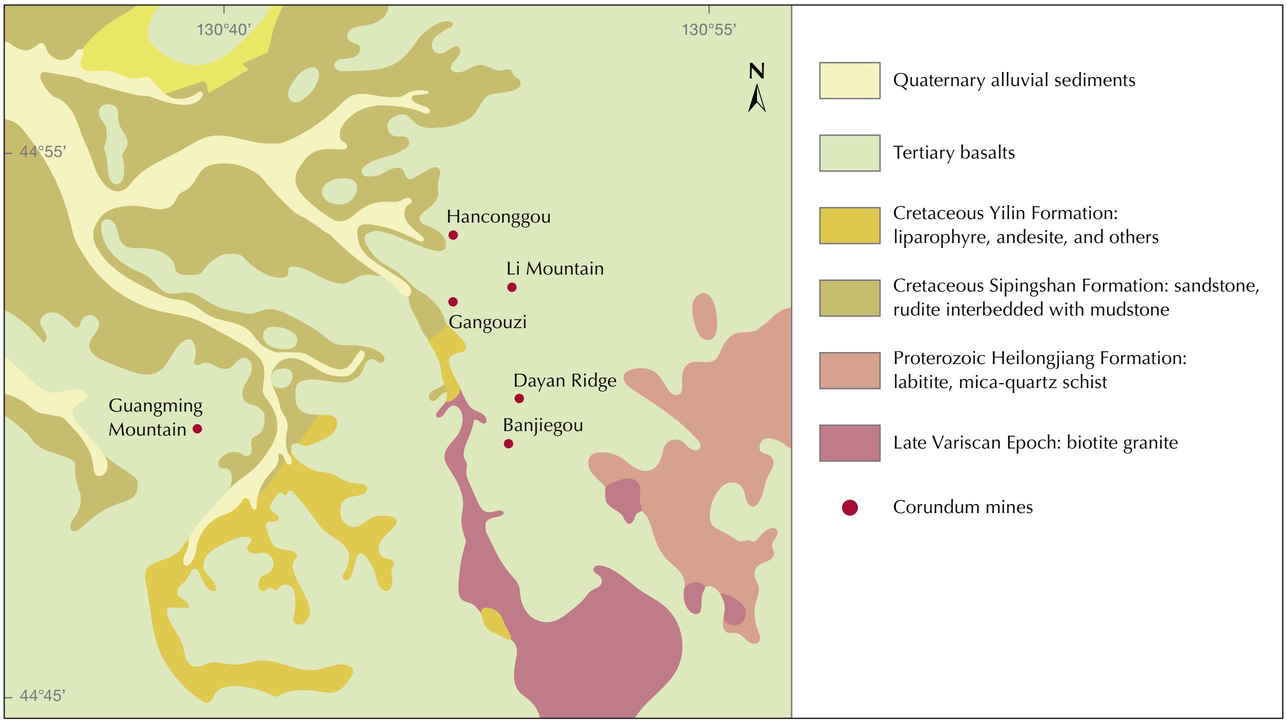

TABLE 1. Number of faceted and wafer samples from each color group of gem corundum from Muling, China.

Color group	Red[a]	Light blue	Deep blue	Yellow	Green	Total number
Wafers	78	43	52	13	10	196
Faceted stones	34	29	36	10	6	115
Wafers for trace element analysis	27	12	17	6	5	67
Faceted stones for trace element analysis	4	1	3	1	1	10

[a] The red group includes pink, orangy pink, purple, and purplish red.

Standard Gemological Testing. Standard gemological testing was performed at the gemological laboratory of the Gemmological Institute, China University of Geosciences in Wuhan. An optical duplex gem refractometer was used to measure the refractive index and birefringence of the polished stones. Fluorescence was observed with long- and short-wave UV lamps (365 and 254 nm, respectively) in a darkened room. Specific gravity was determined hydrostatically with an electronic balance.

Photomicrography. Internal features of the 311 polished wafer and faceted samples were observed and recorded under different magnifications with a Leica M205 A camera and a LAS V4.12 system. Various illuminations including darkfield, brightfield, diffused, and oblique, together with a fiber-optic light source, were utilized as necessary.

Raman Spectroscopy. To identify mineral inclusions, Raman spectra of all 311 samples were obtained at the gemological laboratory of the Gemmological Institute, China University of Geosciences in Wuhan, using a Bruker Senterra R200-L Raman spectrometer fitted with a 532 nm laser and magnifications of 20× and 50×. The laser power was set at 10 mW. The spectra were collected in the confocal mode with a spectral resolution of 5 cm^{-1} and an integration time of 20 s. The accumulation was set at 5 times until the signal-to-noise ratio of the spectra was above 10. Calibration was performed using the 520.5 cm^{-1} line of a silicon wafer. In all cases, the RRUFF database (rruff.info; Lafuente et al., 2015) was referenced when identifying inclusions.

FTIR Spectroscopy. To detect potential trace-level hydrogen in gem corundum and hydrous mineral inclusions, Fourier-transform infrared (FTIR) spectroscopy was performed on all 196 wafered samples using a Bruker Vertex 80 spectrometer equipped with a Hyperion 3000 microscope and a combination of beam splitters and detectors for the mid- to near-infrared ranges (7000–400 cm^{-1}). The magnification of the objective lens was 15×. The spectral resolution was set at 2 cm^{-1} with 64 accumulations.

UV-Vis-NIR Spectroscopy. To illustrate the major chromophores' features, 196 doubly polished wafers covering the main color groups—red (including pink, orangy pink, purple, and purplish red), light blue, deep blue, yellow, and green—were analyzed with ultraviolet/visible/near-infrared (UV-Vis-NIR) spectroscopy using a PerkinElmer 650s spectrometer with a 150 mm integrating sphere accessory. To further clarify the quantitative relationship between trace elements and spectral absorption, samples were further screened and prepared to obtain UV-visible spectra in a more focused sampling area. UV-Vis-NIR spectra were collected using a JASCO MSV-5200 spectrometer equipped with a microscope and a 16× objective. The sampling area of 400 μm diameter covered the same area as the laser spots resulting from laser ablation–inductively coupled plasma–mass spectrometry (LA-ICP-MS) analysis. Spectra were collected in the 300–1500 nm range. The spectral resolution was 0.1 nm with a scan speed of 200 nm/min.

Four deep blue sapphires with high clarity and no noticeable twinning structures (DB2, DB12, DB31, and DB35) were prepared as oriented wafers (perpendicular to the *c*-axis) and further studied for spectra in both orientations and for *in situ* chemical analysis. The optical qualities of samples in other color groups were affected by twinning to various degrees. Samples with moderate or minor twinning were selected and cut into wafers for the analysis of microscopic-scale submillimeter spectroscopy and trace element chemistry. Efforts were made to obtain fully oriented spectra. However, the optical conditions of the crystals did not allow us to precisely determine the orientation of each optic axis due to the twinning. For the red and light blue groups, partially oriented spectra (o-ray) of nine samples were obtained (sample nos. R5, R12, R20, R28, R41, LB3, LB7, LB19, and LB29). For the yellow and green group samples, partial or non-oriented spectra were obtained (sample nos. Y3-7 and G1-5).

The absorbance was first corrected by subtracting the loss of multiple reflections. The Sellmeier equation for corundum was performed to determine a given sample's refractive index and calculate all the reflections between the two surfaces (Tatian, 1984). Except for reflection, the internal scatter of inclusions (Lu, 2012) may impact the spectral baseline of natural corundum samples, unlike the high-purity synthetic corundum materials. Considering the potential near-infrared absorption centered at 880 nm, the spectral baseline was then corrected by subtracting the spectral offset at 1500 nm, where the chromophore's features were insignificant. The spectroscopic data was converted to show absorption coefficient (α, cm^{-1}) using $\alpha = 2.303A/d$, where A is absorbance and d is the path length in centimeters.

Trace Element Analysis. LA-ICP-MS analysis was carried out at the State Key Laboratory of Geological Processes and Mineral Resources, China University of Geosciences in Wuhan. The instrument used was an Agilent 7500 ICP-MS combined with a GeoLas 193 nm laser. Laser ablation conditions included a 44 μm diameter laser spot size, a fluence of 12 J/cm^2, and a 6 Hz repetition rate. Each analysis incorporated a background acquisition of approximately 20 s (gas blank), followed by 50 s of main acquisition time and 30 s of washout phase. Three spot analyses were performed on each sample. The widely used quantitative calibration standards of National Institute of Standards and Technology (NIST) glass SRM 610 and U.S. Geological Survey (USGS) synthetic glasses BCR-2G, BHVO-2G, and BIR-1G (Jochum et al., 2005) were used as reference materials. The preferred values of element concentrations for the USGS reference glasses are from the GeoReM database (http://georem.mpch-mainz.gwdg.de). Each analysis was first normalized by aluminum, and then a time-drift correction was applied using a linear interpolation (with time) for every nine analyses according to the variations of SRM 610 (Liu et al., 2008). Offline selection, integration of background, analyte signals, and quantitative calibration were performed by ICPMSDataCal (Liu et al., 2008).

Units of ppmw and ppma were both used for the trace element content in this study. The unit ppmw was applied in the discrimination diagrams. One ppmw means that there is one microgram of trace element in one gram of crystal. The unit ppma was applied to discuss the impact of trace elements on coloration. One ppma means that there is one trace element atom for every million atoms of the host crystal (Emmett et al., 2003).

RESULTS

Sample Grouping Rules. Grouping of samples was mainly based on dominant chromophore series: Cr^{3+} for red (including pink, orangy pink, purple, and purplish red), Fe^{2+}-Ti^{4+} pair for blue, and Fe^{3+} for yellow. Samples in the Fe^{2+}-Ti^{4+} series were further divided into light and deep blue, which exhibited differences in their crystal morphology and inclusion scenes and suggested differences in geological formation processes. Samples with Fe^{3+} and combined chromophores of Fe^{3+} and Fe^{2+}-Ti^{4+} were separated into yellow and green categories, respectively. Analytical data from spectroscopy and trace element chemistry are presented following the above chromophore categories.

Gemological Properties. The Muling gem corundum samples in this study covered a wide spectrum of hue, encompassing blue, green, yellow, and red series (including pink, orangy pink, purple, and purplish red) and saturation ranging from light to deep. Samples were divided into five groups according to the grouping rules above. Deep blue sapphire refers to those with a strong saturation (e.g., the faceted blue sapphire in the bottom center of figure 1). By contrast, the light blue sapphire material had lower saturation and high transparency. Other color groups (red, yellow, and green) were within a narrower range of saturation than the spread between the deep blue and light blue groups. In addition to the grouping mentioned above, there were a few distinctively bicolor samples (less than 0.1%) that combined deep blue and yellow within a single stone.

Samples in the different color groups generally displayed distinct crystal morphology. Samples with high saturation (i.e., those in the deep blue group and the green group, and the very few deep blue and yel-

Figure 7. Rough stones from Muling, representing the five color groups from this study: two light blue sapphires (top left), four deep blue sapphires (bottom left), seven from the red group (including pink and purple samples; right), one green sample (bottom center), and one yellow sample (bottom right). The deep blue sapphires displayed well-developed barrel or tabular crystal shapes and predominantly hexagonal prisms. The light blue sapphires showed rounded shapes and erosion surfaces, while the red group consisted mainly of broken pieces with erosion surfaces or tabular crystals. The green and yellow samples were all broken pieces. Photo by Yimiao Liu.

low bicolor samples) showed little effect from weathering and appeared mainly as broken pieces with relatively sharp edges or retained their original crystal shapes. Most of the deep blue rough exhibited euhedral and subhedral crystal shapes (such as barrel or tabular) with hexagonal prisms as the dominant crystal form (figure 7). Some showed six-ray trapiche patterns. The red group samples mainly displayed tabular rounded morphology, while a few showed a euhedral hexagonal shape. For the light blue and yellow groups, the rough stones usually exhibited erosion surfaces with rounded shapes.

Among all the samples collected from Muling, the largest rough stone reached 51 ct (a deep blue sample), with the weight of most stones in the 1–3 ct range. The calculated proportions for each color group are provided in figure 8. The red group samples (including pink, orangy pink, purple, and purplish red) made up the largest proportion of all Muling gem corundum, at 57%. Light blue and deep blue sapphires accounted for 15% and 16%, respectively. Yellow sapphires made up 6% of all samples, and green sapphires accounted for 3% (figure 8).

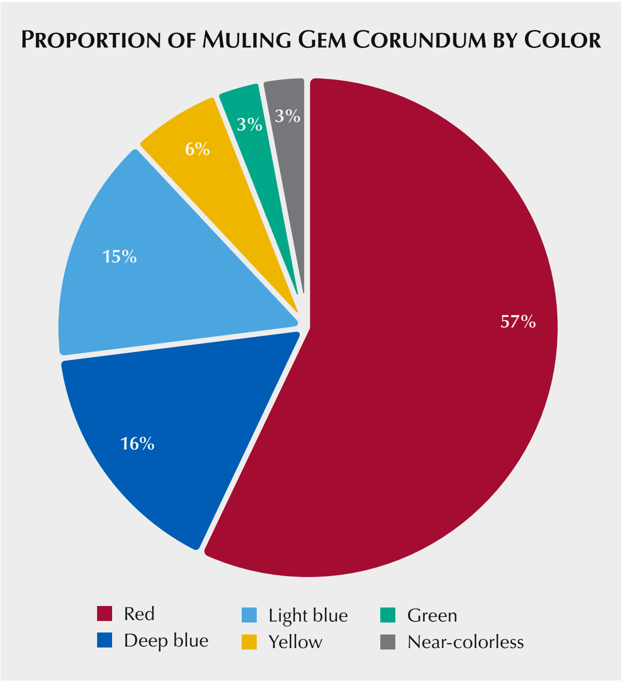

Figure 8. A pie chart of the five color groups (plus near-colorless) among the randomly selected ~1,030 Muling corundum samples. Among them, the red group (pink, orangy pink, purple, and purplish red) has the largest share, with 57%. Deep blue and light blue samples account for 16% and 15%, respectively. The rest consist of yellow, green, and near-colorless samples (6%, 3%, and 3%, respectively).

TABLE 2. Gemological characteristics of studied wafer and faceted gem corundum samples from Muling, China.

Color group		Red[a]	Light blue	Deep blue	Yellow	Green
Number of samples		112	72	88	23	16
Transparency		Transparent to semitransparent	Transparent to semitransparent	Transparent to semitransparent	Transparent	Transparent
Refractive index	n_o	1.758–1.760	1.758–1.760	1.760–1.762	1.759–1.762	1.760–1.762
	n_e	1.769–1.771	1.768–1.771	1.768–1.770	1.768–1.770	1.768–1.770
Birefringence		0.008–0.009	0.008–0.010	0.008	0.008	0.008
Dichroism		Medium: pink to purplish red	Medium: light blue to blue	Strong: blue to greenish blue	Weak: yellow to colorless	Strong: green to bluish green
Specific gravity		3.99–4.00	3.97–4.12	3.98–4.00	3.97–4.10	3.97–4.05
Fluorescence		Long-wave: Medium red Short-wave: Weak red	Inert	Inert	Inert	Inert

[a]The red group includes pink, orangy pink, purple, and purplish red.

Gemological characteristics by color group are summarized in table 2. The sample clarity ranged from transparent to semitransparent. Those crystals with high clarity and desirable color exhibited obvious commercial potential after cutting (again, see figure 1). Refractive index ranged from 1.760 to 1.769, and specific gravity was around 4.0 ± 0.2. Samples in the red group showed medium red fluorescence under long-wave UV radiation and weak red under short-wave UV. Other color groups were inert under both long-wave and short-wave UV.

Internal Features. Representative photos were chosen to exhibit both common and rare internal features of the Muling sapphire after thoroughly examining the 311 faceted and wafer samples and documenting their microscopic characteristics.

Microscopic examination combined with Raman spectroscopy revealed various mineral inclusions such as rutile, zircon, anorthite, and pyrope. Rutile needles were the most common mineral inclusion, occurring in a short arrowhead shape and displaying iridescence along certain orientations (see figure 9;

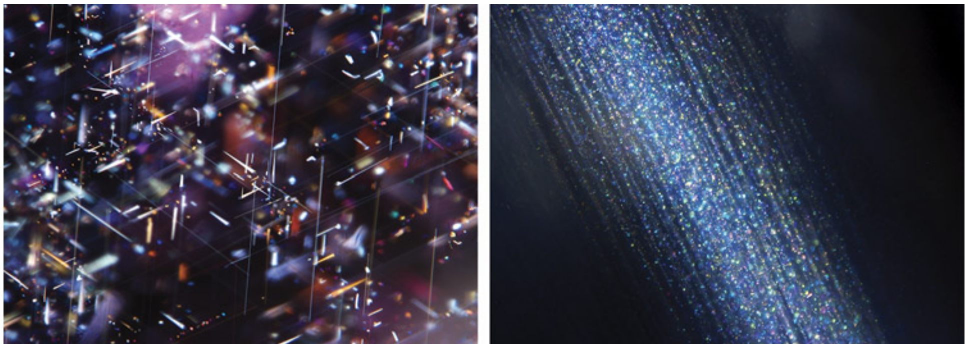

Figure 9. Left: Long silk and short arrowhead needles in a pink sapphire, at 60°/120° angles. Right: Densely packed reflective particles in a light blue sapphire observed under oblique illumination. Photomicrographs by Yimiao Liu; fields of view 0.98 and 1.56 mm, respectively.

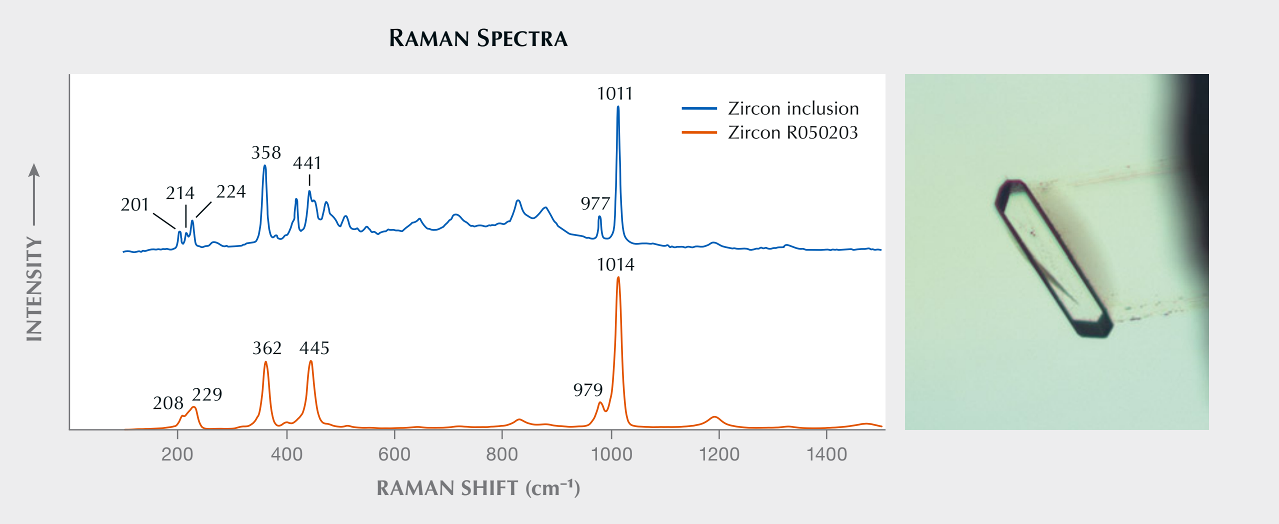

Figure 10. The Raman spectrum of a zircon inclusion in a deep blue sapphire sample matched the reference spectrum for zircon in the RRUFF database. Spectra are offset vertically for clarity. The inclusion is shown in the inset photo. Photomicrograph by Yimiao Liu; field of view 0.31 mm.

this inclusion image comes from the top middle purple sapphire in figure 1). Long silk was also common in Muling sapphire.

Zircon inclusions were occasionally encountered in deep blue sapphire. These were transparent, well-developed prismatic crystals (figure 10), typically isolated and rarely clustered. Most of them measured up to 200 µm long.

Prismatic and rounded, transparent calcium-rich plagioclase crystals (whose Raman spectra matched with anorthite) were discovered in a number of light blue sapphires (figure 11). Both the mineral identity and crystal morphology suggest a protogenetic origin (Koivula and Fryer, 1987).

Garnet, identified by Raman spectroscopy as pyrope, rarely occurred as an inclusion and was only observed in two stones from the red group and one from the yellow group, all with well-developed crystal forms (figure 12). The size measured up to 200–300 µm.

An unusual multicomponent inclusion was discovered in one purplish red sample. Micro-sized clus-

Figure 11. The Raman spectrum of an anorthite crystal inclusion observed in a Muling light blue sapphire matched the reference spectrum for anorthite in the RRUFF database. Spectra are offset vertically for clarity. The inclusion is shown in the inset photo. Photomicrograph by Yimiao Liu; field of view 0.20 mm.

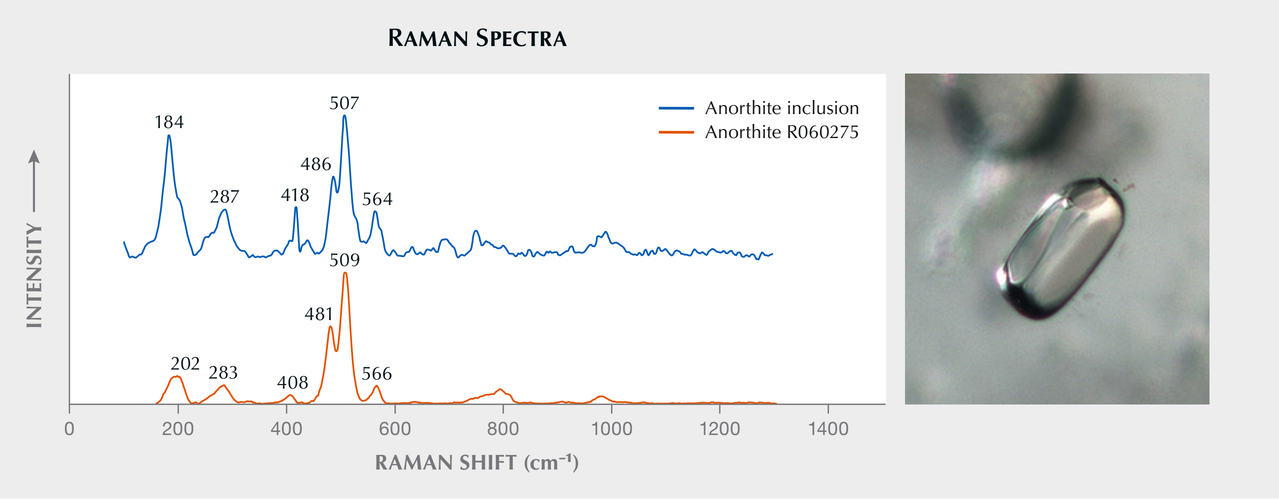

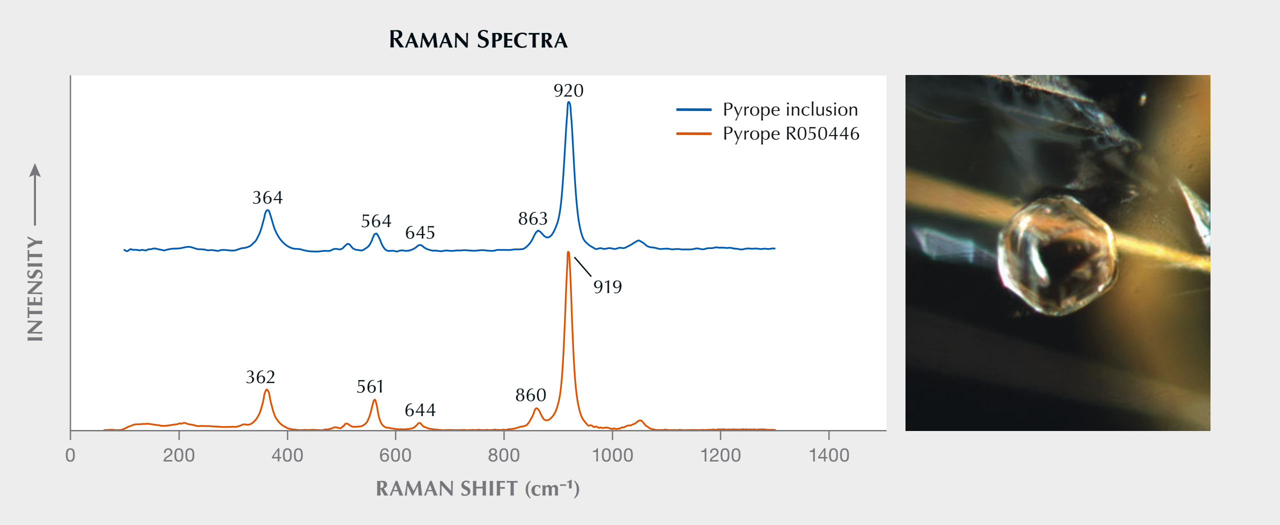

Figure 12. The Raman spectrum of a garnet inclusion observed in a Muling yellow sapphire matched the reference spectrum for pyrope in the RRUFF database. Spectra are offset vertically for clarity. The inclusion is shown in the inset photo. Photomicrograph by Yimiao Liu; field of view 0.59 mm.

ters of crystals arranged in different orientations were observed inside a hexagonal negative crystal (figure 13). Various clusters had different Raman spectra. The spectra for points A and B matched with sillimanite

Figure 13. The Raman spectra of a multicomponent inclusion observed in a Muling purplish red sample, identified using Raman spectroscopy and referencing the RRUFF database. Spectra are offset vertically for clarity. The spectrum of point A matched sillimanite, while point B matched anorthite. Double peaks near 700 cm^{-1} were present in the corundum matrix and in the other regions of this corundum sample and are not from inclusions. The inclusion is shown in the inset photo. Photomicrograph by Yimiao Liu; field of view 0.15 mm.

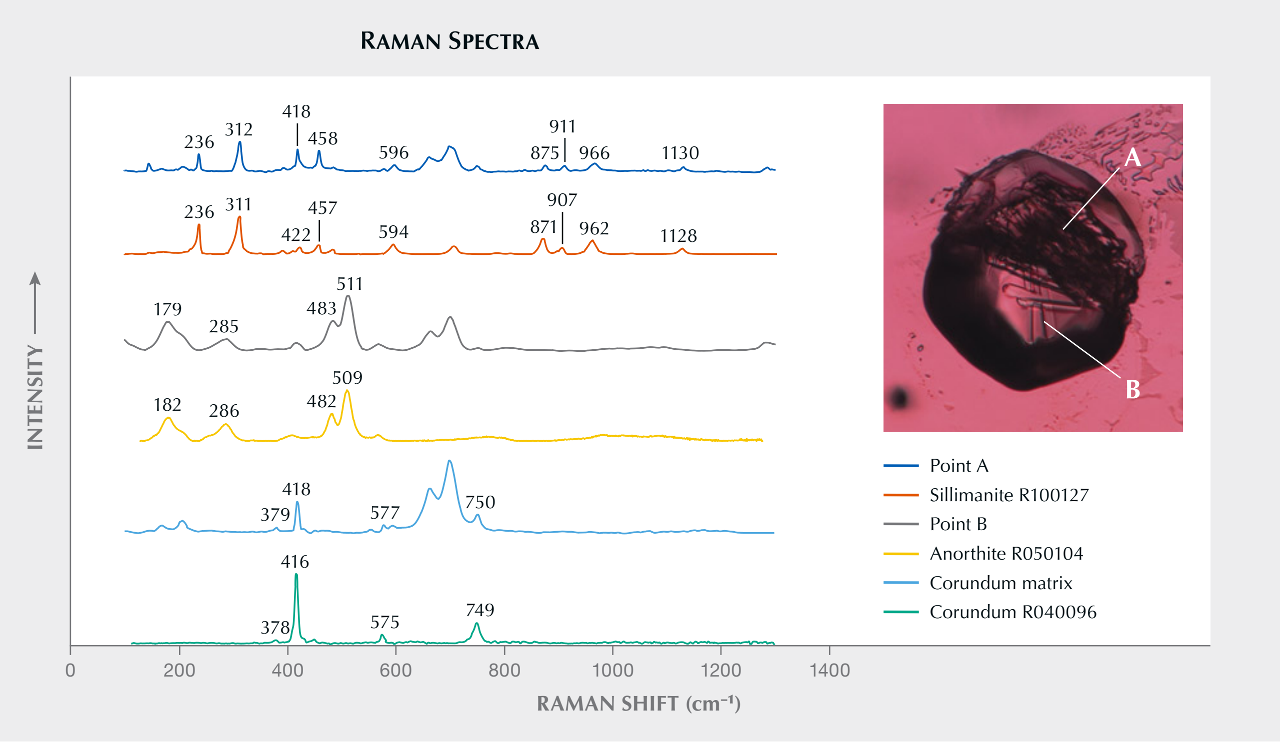

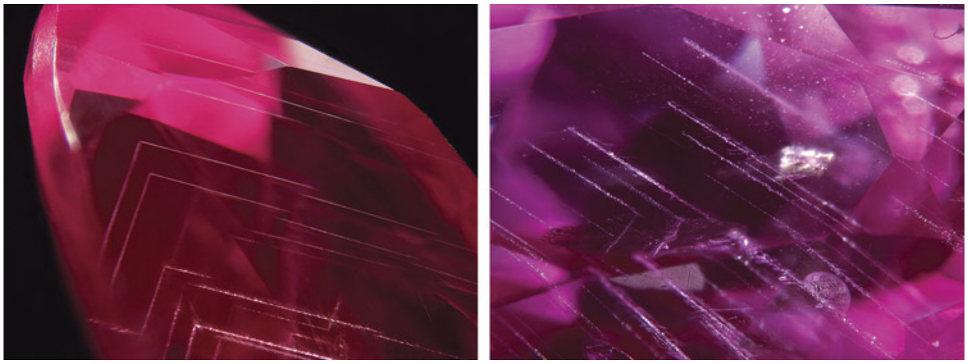

Figure 14. Left: Unidentified whitish linear inclusions intersect in an angular-shaped pattern in a Muling purple sample; field of view 3.16 mm. Right: A pink sapphire showed subparallel dotted lines with fringes; field of view 3.25 mm. Photomicrographs by Yimiao Liu.

Figure 15. Left: Between crossed polarizers, this purple sample shows polysynthetic twinning. The inner-lamellar spacing measured ~0.9 mm. Right: A doubly polished purple sapphire wafer shows two sets of twinning planes with a 54° angle under cross-polarized light. Photos by Yimiao Liu.

and anorthite, respectively. These two cluster types were most likely daughter minerals that crystallized from the included fluids as temperature decreased.

Whitish linear inclusions were frequently observed in red and light blue samples. They occurred in specific directions: subparallel or intersecting with each other (figure 14). Magnification showed dotted lines with fringes (figure 14, right). These linear features were not positively identified by FTIR and Raman spectroscopy. Polysynthetic twinning was also common in red and light blue samples (figure 15). Under cross-polarized light, multiple sets of twinning sometimes intersected with each other where linear inclusions occurred along the intersections (figure 15, right).

Figure 16. Well-defined hexagonal color zones in this deep blue stone indicate the crystallization process of the host sapphire. Photomicrograph by Yimiao Liu; field of view 3.94 mm.

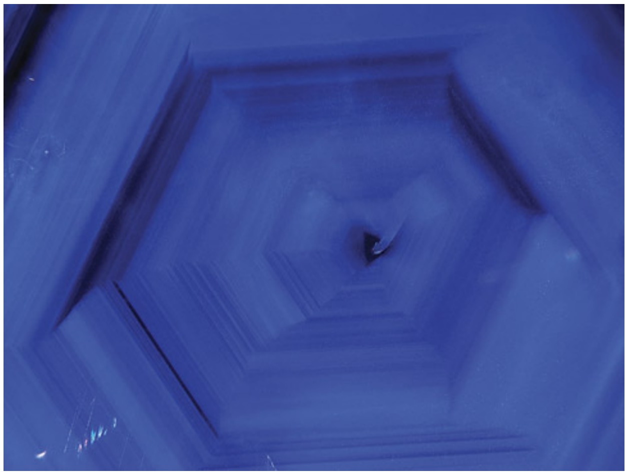

There are some other notable internal features in Muling sapphire. Angular color zoning was observed only in deep blue sapphire (figure 16), which has not been observed in the other color groups.

Thin films occurred in both green and light blue sapphires (figure 17). Their hexagonal shapes or angular iridescent patterns were closely related to the crystallographic symmetry of the host sapphire. All of the thin films reflected light at the same time because the crystal planes were identically oriented. Most were accompanied by a round elongated inclusion in the center. However, Raman spectroscopy failed to positively identify this type of inclusion.

Fissures and fingerprints as secondary inclusions were usually observed in the edge area of rough stones (figure 18, left). Triangular growth features were also common on the surfaces of samples from all color groups (figure 18, right).

Figure 17. Left: An elongated crystal inclusion within a thin-film decrepitation halo in a green sapphire, showing a geometric distribution of interference colors; field of view 0.42 mm. Right: An orthohexagonal thin film conforming to the sapphire's crystal symmetry; field of view 0.86 mm. Photomicrographs by Yimiao Liu.

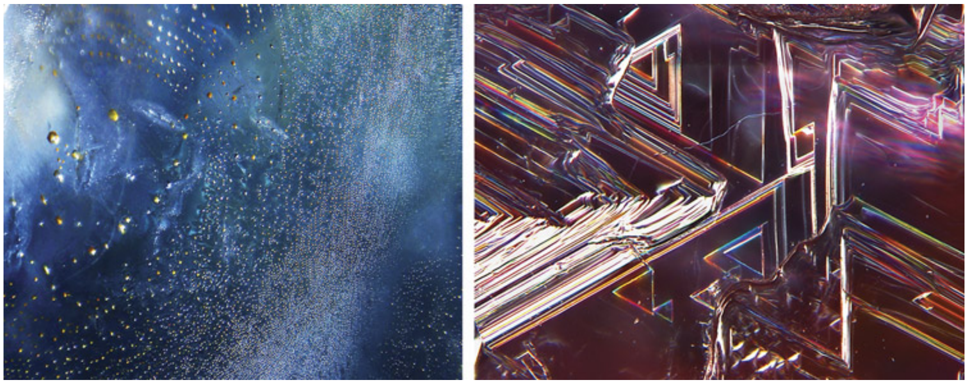

Figure 18. Left: Fingerprints with tiny negative crystals in a light blue sapphire, observed under oblique illumination; field of view 1.82 mm. Right: Surface details of a pink sapphire, showing triangular crystal growth terraces; field of view 2.28 mm. Photomicrographs by Yimiao Liu.

FTIR Spectral Features. FTIR spectroscopy was performed on 196 wafer samples in each color group. Ten percent of 52 deep blue wafers studied displayed peaks at 3310 and 3233 cm^{-1} (see sample DB3 in figure 19), which can be assigned to the intrinsic OH defects (Beran and Rossman, 2006). Nevertheless, 90% of deep blue samples and samples from other color groups showed no significant peaks (again, see figure 19).

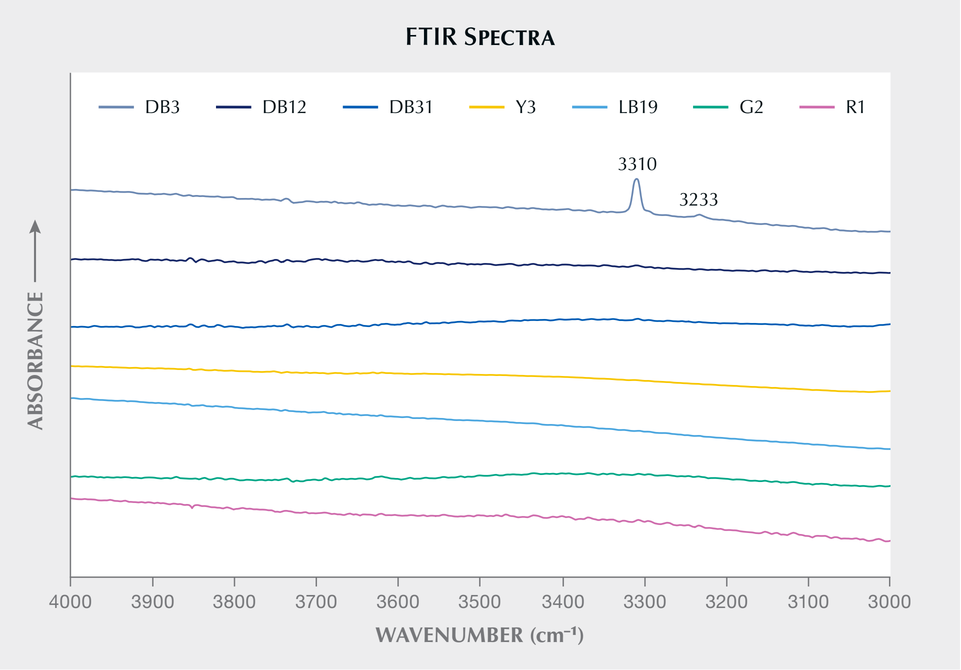

Figure 19. The FTIR spectra of representative samples from each group. Samples DB3, DB12, and DB31 were selected to represent the deep blue group, in which DB3 displayed sharp peaks at 3310 and 3233 cm^{-1}. Samples Y3, LB19, G2, and R1 represented other groups with no significant peaks shown in the 4000–3000 cm^{-1} range. Spectra are offset vertically for clarity.

TABLE 3. Concentrations of key trace elements in gem corundum from Muling, China.

Color group	Red[a]		Light blue		Deep blue		Yellow		Green		
Number of samples	31		13		20		7		6		
Number of analyses	102		42		72		24		21		
Trace elements	Range	Mean	Range	Mean	Range	Mean	Range	Mean	Range	Mean	Detection limits
ppmw[b]											
Mg	21–139	60	27–182	86	bdl[c]–212	40	5–71	34	33–63	49	3
Ti	16–203	74	28–261	128	41–1162	323	5–199	52	51–90	72	1.5
V	bdl–49.3	14.6	3.3–59.7	23.6	bdl–75.3	30.5	1.4–9.6	4.9	3.1–41.9	16.2	0.2
Cr	140–10274	970	bdl–293	35	bdl–74	14	bdl–94	30	bdl–33	9	4.9
Fe	1939–7192	4251	2948–9133	5651	1834–13162	4958	4530–12151	7155	4753–8337	6380	25
Ni	bdl–46	—	bdl–56	6	bdl–31	—	bdl–848[d]	71	bdl–12	—	4.5
Ga	21.6–56.9	37.2	23.0–75.5	41.9	119.8–201.9	158.8	20.2–336.2	115.7	28.6–69.3	42.4	0.6
ppma[e]											
Mg	17–113	49	22–149	70	bdl–173	33	4–58	28	27–51	40	2
Ti	7–88	32	12–113	54	17–505	137	2–86	22	21–39	31	0.7
V	bdl–19.7	5.9	1.3–23.9	9.4	bdl–30.1	12.2	0.6–3.8	1.9	1.3–16.8	6.5	0.08
Cr	54–3958	329	bdl–113	14	bdl–28	6	bdl–36	12	bdl–13	4	1.9
Fe	695–2576	1523	1056–3271	2024	657–4714	1776	1623–4352	2563	1702–2986	2285	9
Ni	bdl–16	—	bdl–19	2	bdl–10	—	bdl–288	24	bdl–4	—	1.5
Ga	6.2–16.4	10.7	6.6–21.7	12.0	34.4–58.1	45.7	5.8–96.7	33.3	8.2–19.9	12.2	0.2

[a] The red group includes pink, orangy pink, purple, and purplish red.

[b] ppmw = parts per million by weight or μg/g

[c] bdl = below the detection limit of the analysis; mean values below the relevant detection limits are omitted.

[d] One abnormal high nickel value for yellow might have been caused by the instability of the instrument.

[e] ppma = parts per million atomic; $ppma = \frac{(molecular\ weight\ of\ Al_2O_3)/5}{atomic\ weight\ of\ the\ element} \times ppmw$

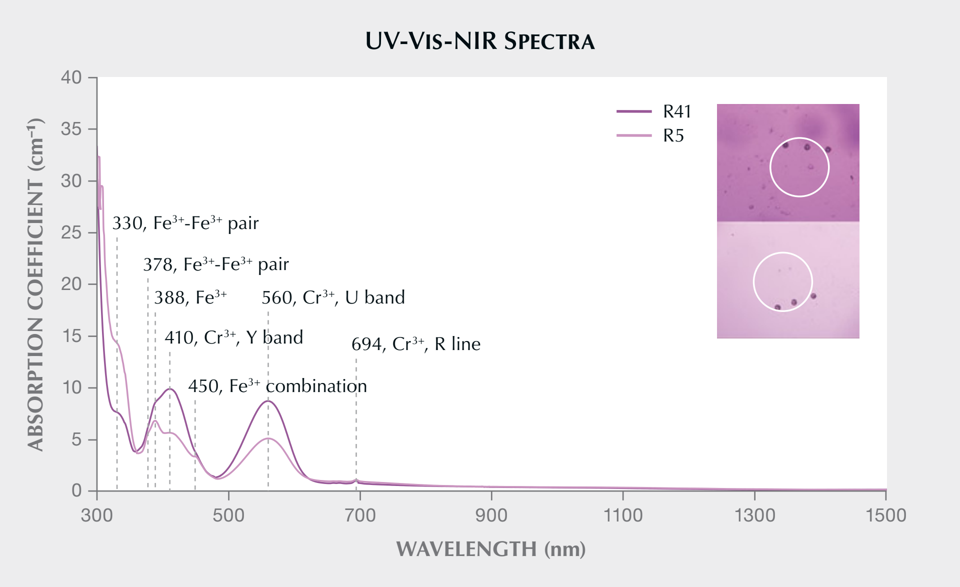

Figure 20. UV-Vis-NIR spectra comparing two pink sapphires with different saturations (sample nos. R41 and R5). The areas analyzed are shown in the inset photos, indicated by the white circles (400 µm diameter).

Chemical Analysis. Seventy-eight samples from Muling were measured by LA-ICP-MS, and the trace element composition varied according to bodycolor. Table 3 shows regular concentrations and atomic concentrations of trace elements (magnesium, titanium, vanadium, chromium, iron, nickel, and gallium) that may directly or indirectly impact the samples' coloration or origin determination (for individual stone data, see supplementary information at https://www.gia.edu/gems-gemology/fall-2022-sapphire-from-china). Value ranges and corresponding mean values and detection limits are displayed in this table. Elements such as magnesium, titanium, vanadium, iron, and gallium, although with various concentrations, occurred in all groups regardless of color, while chromium occurred mainly in the red group. When the average value of elements was below the relevant detection limit, the data was omitted. Some isotopes such as ^{9}Be, ^{90}Zr, ^{93}Nb, and ^{181}Ta displayed detectable values near detection limits sporadically, with one or two spots among all data. It is likely that laser-ablated microscopic particulates contained these elements (Lu and Shen, 2011; Pardieu, 2013; Emori et al., 2014). This data is not presented in table 3 because it is not directly related to the corundum.

Other measured isotopes (^{7}Li, ^{11}B, ^{45}Sc, ^{55}Mn, ^{59}Co, ^{66}Zn, ^{85}Rb, ^{88}Sr, ^{89}Y, ^{97}Mo, ^{118}Sn, ^{133}Cs, ^{137}Ba, ^{139}La, ^{140}Ce, ^{146}Nd, ^{147}Sm, ^{153}Eu, ^{178}Hf, ^{182}W, and ^{232}Th) were generally below detection limits or less than a few ppmw. Although silicon is common in corundum (Emmett et al., 2017), it is beyond the scope of this article due to the poor detection limit caused by the mass interference. Furthermore, the explanation of coloration would be affected by the unaccounted incorporation of Si^{4+}.

UV-Vis-NIR Spectral Features. The main color hues and saturations of Muling sapphire were examined using quantitative UV-Vis-NIR spectroscopy. Data were collected in the range extending to 1500 nm in the infrared region, beyond which no known chromophores exist (see, e.g., figure 22). All trace element analyses were performed over the spectrally analyzed local areas. The two sets of data (spectral and chemical) are highly correlated via the application of a UV-visible spectrometer equipped with a microscope. The real chromophore mechanisms of samples from each color group were then determined according to the rules of impurity interactions in corundum (Emmett et al., 2003, 2017).

Red Group (Pink, Orangy Pink, Purple, and Purplish Red Sapphire). The main chromophore features of red group samples in different saturations are shown in figure 20. Non-oriented UV-Vis-NIR spectra were acquired due to the twinning structures in the red group samples. Pink sapphires R5 and R41, with chromium contents of 197 and 473 ppma, respectively, were selected as representative of the red group to demonstrate variations in saturation. As seen in figure 20, these absorption spectra show evident Cr^{3+} features (i.e., Y band at 410 nm, U band at 560 nm, and R-line at 694 nm; Powell, 1998) superimposed by the Fe^{3+} absorptions (peaks at 378, 388, and 450 nm and a shoulder at 330 nm; Ferguson and Fielding, 1971 and 1972). The heights of the U band and Y band are positively associated with chromium content (table 4). Since the Fe^{2+}-Ti^{4+} pair is an effective chromophore with a strong absorption cross section (Dubinsky et

TABLE 4. Trace element compositions (in ppma) of representative red group samples (R41 and R5) from Muling, China.[a]

Sample no.	Mg	Ti	V	Cr	Fe
R41	27 (4)	12 (1)	3.4 (0.2)	473 (7)	910 (11)
R5	30 (1)	15 (2)	3.3 (0.4)	197 (5)	1821 (34)

[a]Average concentrations of three LA-ICP-MS data in each sample are shown with the standard deviation (ppma) in parentheses.

al., 2020), concentrations of a few ppma will produce observable coloration. The titanium in these two samples with concentrations above 10 ppma (table 4) showed little effect on the spectra, perhaps due to the existence of magnesium (Emmett et al., 2003, 2017). Low amounts of other elements such as vanadium (table 4) had limited effect on the spectra.

Light Blue Group. After carefully examining all 43 light blue samples, the absorption spectra showed relatively consistent characteristics, as represented by sample LB19 (figure 21). Only non-oriented spectra were acquired because of the twinning structure in this group. The UV-Vis-NIR spectrum of LB19 displayed typical Fe^{3+} absorptions (Ferguson and Fielding, 1972; Hänni, 1994) as well as evident Fe^{2+}-Ti^{4+} intervalence charge transfer absorption (i.e., Fe^{2+}-Ti^{4+} IVCT, band center at approximately 580 nm). The trace element composition of LB19 demonstrates that the sample contains 100 ppma titanium, 2264 ppma iron, and 142 ppma magnesium (table 5). The elements that could cause the sample to produce a blue color (i.e., titanium and iron) are all present in significant concentrations. And such concentration (i.e., 100 ppma, if all titanium is paired with iron) of the Fe^{2+}-Ti^{4+} pair would produce a strong saturation (Dubinsky et al., 2020). However, both the visual appearance and the absorption coefficient of the Fe^{2+}-Ti^{4+} IVCT indicated a weak coloration of the stone. This is most likely due to the presence of the element magnesium. According to the rules of impurity interactions in corundum (Emmett et al., 2003, 2017), titanium will preferentially pair with magnesium before iron. In this case, the atomic content of the magnesium (142 ppma) is higher than that of titanium (100 ppma). If all the titanium paired with

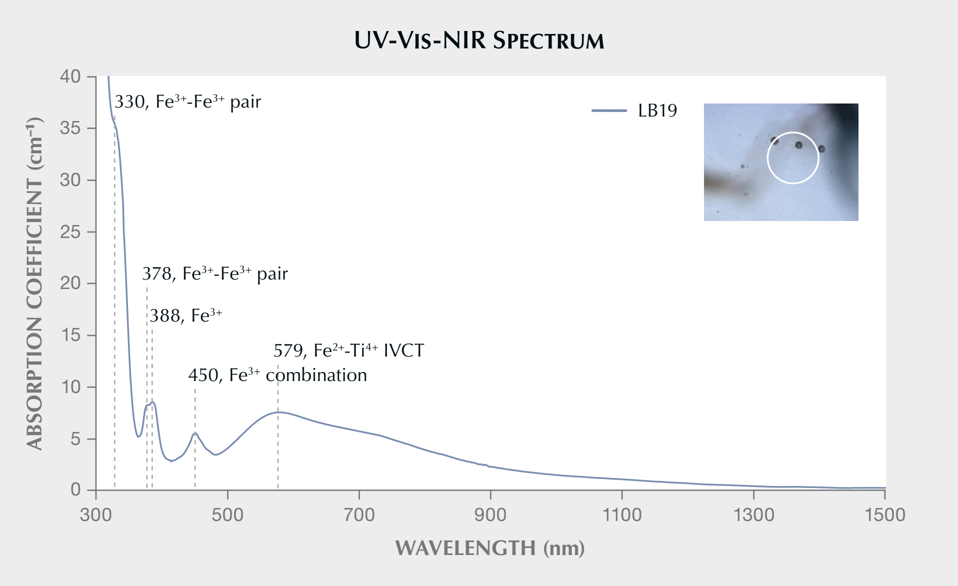

Figure 21. UV-Vis-NIR spectrum of sample LB19 representing the chromophore features of the light blue group. The area analyzed is shown in the inset photo, indicated by the white circle (400 µm diameter).

TABLE 5. Trace element composition (in ppma) of the light blue sapphire LB19 from Muling, China.[a]

Sample no.	Mg	Ti	V	Cr	Fe
LB19	142 (5)	100 (2)	4.2 (0.3)	4 (1)	2264 (49)

[a] Average concentrations of three LA-ICP-MS data of trace elements are shown with the standard deviation (ppma) in parentheses.

magnesium, the stone would theoretically exhibit no blue color and there would be no absorption at 580 nm. Therefore, elements (such as silicon) with higher energy levels than titanium probably exist in the crystal lattice and preferentially pair with magnesium, allowing the remaining titanium to pair with iron and produce a light blue color.

Deep Blue Group. The high clarity and homogeneous structure without twinning of the 52 Muling deep blue sapphires allowed us to prepare high-quality oriented wafers. Therefore, oriented quantitative spectra could be obtained in both o-ray and e-ray directions for the full range from 300 to 1500 nm. Two different types of UV-Vis-NIR spectra were found among all tested spectra of deep blue sapphire wafers. Both types of spectra exhibited significant Fe^{2+}-Ti^{4+} pair features and Fe^{3+} features in the ultraviolet and visible regions. Oriented UV-Vis-NIR spectra of the first type, as represented by sample DB31, are displayed in figure 22. This type is the most common in more than 90% of the 52 deep blue wafers, with a strong and wide band in the near-infrared region (centered at 880 nm). This strong absorption is a typical feature of basalt-related sapphire (Smith, 1978). Figure 23 shows the oriented UV-Vis-NIR spectra of sample DB12, which illustrates the second type of spectra. Observed in less than 10% of deep blue samples, this second type of spectra lacks the strong absorption in the near-infrared region.

The absorption coefficients for the 580 nm band were similar for samples DB31 and DB12. In oriented quantitative spectra, the height of a certain absorption is related to the chromophore concentrations, as the two stones are both deep blue with similar saturation. This suggests that the true Fe^{2+}-Ti^{4+} IVCT concentrations are of similar levels. Combined with the trace element data (table 6), sample DB31 has contents of 224 ppma titanium, 1694 ppma iron, and 16 ppma magnesium. When magnesium content is scarce and titanium content is sufficient to pair with iron, a strong absorption occurs and a deep color is produced.

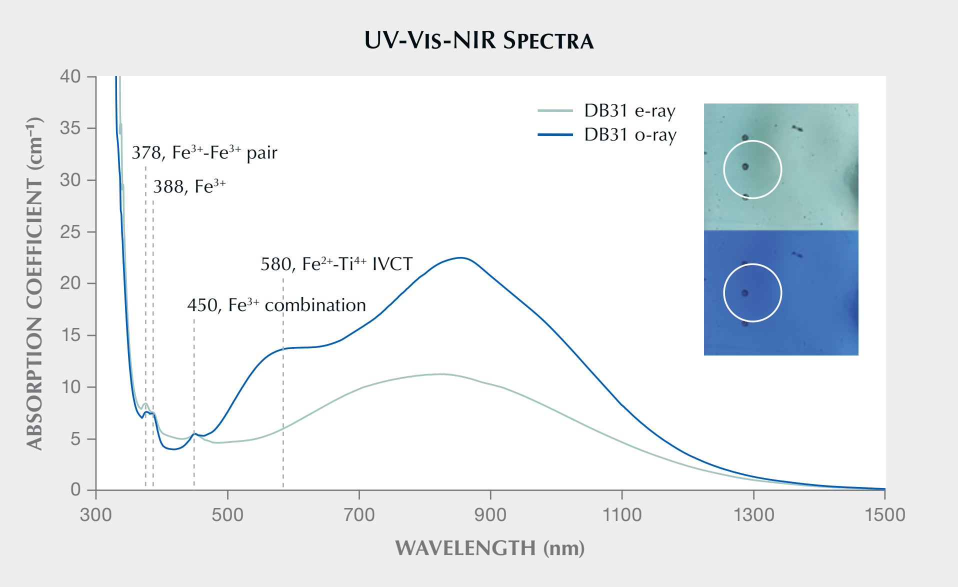

Figure 22. Oriented UV-Vis-NIR spectra of sample DB31 representing features of the first type of spectrum from the deep blue group, with inset photos of the different directions. The white circles indicate the areas analyzed (400 µm diameter).

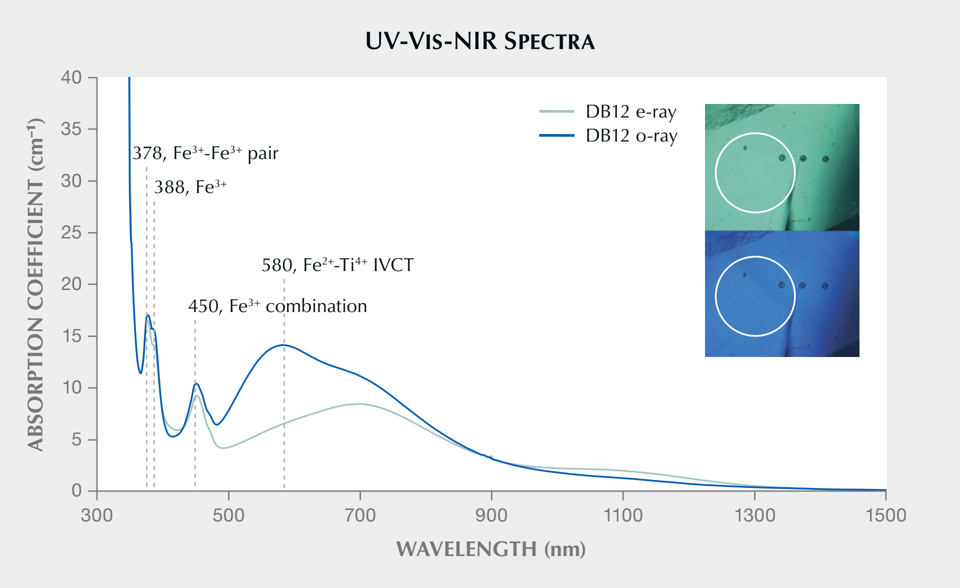

Figure 23. Oriented UV-Vis-NIR spectra of sample DB12 representing features of the second type of spectrum from the deep blue group, with inset photos showing the different directions. The white circles indicate the areas analyzed (400 µm diameter).

The trace element compositions of sample DB12 showed contents of 149 ppma titanium, 3690 ppma iron, and 169 ppma magnesium. The atomic concentrations of magnesium were analyzed to be higher than the concentrations of titanium. The high color saturation of this deep blue sapphire, caused by Fe^{2+}-Ti^{4+} IVCT, implies a large amount of titanium paired with iron instead of magnesium. It is deduced that there is a large depletion of magnesium by silicon. Furthermore, the weak bands at 700 and 1100 nm in the oriented spectra of sample DB12 (figure 23) might be related to the high Fe^{3+} concentrations (Dubinsky et al., 2020). LA-ICP-MS confirmed sample DB12's iron concentration of 3690 ppma (table 6).

Yellow and Green Groups. Samples in the yellow and green groups mainly exhibited Fe^{3+} features in their non-oriented UV-Vis-NIR spectra. Samples Y3 and G5 were selected as representative to exhibit the chromophore features (figure 24). The spectrum of yellow sapphire (sample Y3) showed weak absorption in the visible light region with mainly Fe^{3+} features and a weak broad band at 570 nm. Compared to the yellow sample, the green sapphire (sample G5) showed relatively strong absorptions at Fe^{3+} peaks (377, 388, and 450 nm) and the 570 nm band (which might be associated with the V^{3+} transition; Schmetzer and Bank, 1981), giving the stone a bluish green hue. The trace element data of these two samples (table 7) showed consistent results in their spectra, with iron the most significant impurity in both samples. Other elements showed only minor concentrations in both the yellow and green samples. The existence of vanadium and titanium in sample G5 might be the reason for the absorption at 570 nm, which would cause the green hue to appear.

TABLE 6. Trace element composition (in ppma) of two deep blue sapphires (DB31 and DB12) from Muling, China.[a]

Sample no.	Mg	Ti	V	Cr	Fe
DB31	16 (4)	224 (10)	6.7 (0.3)	0 (0)	1694 (47)
DB12	169 (4)	149 (3)	20.9 (0.5)	15 (2)	3690 (92)

[a] Average concentrations of three LA-ICP-MS data in each sample are shown with the standard deviation (ppma) in parentheses.

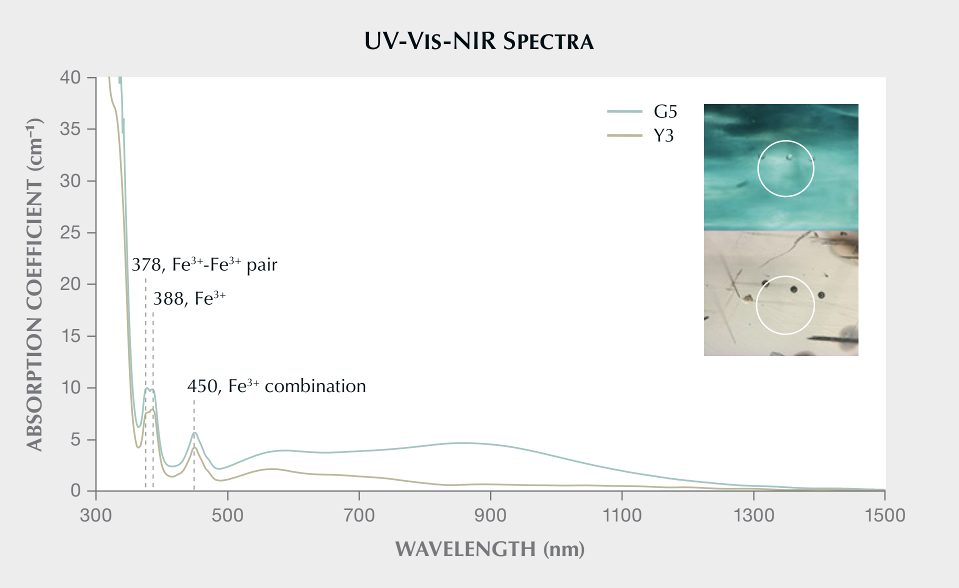

Figure 24. UV-Vis-NIR spectra comparing a yellow and a green sample (sample nos. Y3 and G5) from Muling. The areas analyzed are shown in the inset photos, indicated by the white circle (400 µm diameter).

DISCUSSION

Provenance Characteristics of Muling Sapphire. Muling sapphire comes in a wide range of colors and can display vivid color and high clarity, unlike sapphire from other magmatic deposits in China (Guo et al., 1992; Wang et al., 1992; Cheng et al., 2009; Zhang et al., 2018). The high color saturation of unheated Muling sapphire also reveals distinctive appearances compared to Montana sapphire (Emmett and Douthit, 1993; Hsu et al., 2017). The appearance is comparable to sapphire from other classic deposits such as Thailand or Madagascar. Therefore, additional evidence is needed to identify the provenance features of Muling sapphire.

Internal Features. Mineral inclusions in the Muling samples consisted of short rutile needles, euhedral prismatic zircon crystals, rounded prismatic calcium-rich plagioclase, and garnet. These internal features (figures 9–15) are essential evidence of geographic origin. Comparison with published papers and the GIA classification system (https://www.gia.edu/corundum-report-cover-source-type) confirms that Muling sapphire inclusions overlap with typical metamorphic and magmatic sapphires.

Long to short rutile needles were common in samples of almost all colors except for yellow (table 8). Short arrow-headed needles, which were mainly encountered in light blue and red group samples from Muling, are regarded as the hallmark of Burmese origin and classic in Madagascar sapphire (Palke et al., 2019a,b) (table 5). However, rutile cannot be considered a decisive indicator of locality, as it is known to occur in corundum from various geological origins (e.g., Gübelin and Koivula, 1986; Palke et al., 2017, 2019a).

TABLE 7. Trace element composition (in ppma) of a yellow sapphire (Y3) and a green sapphire (G5) from Muling, China.[a]

Sample no.	Mg	Ti	V	Cr	Fe
Y3	41 (1)	20 (2)	2.2 (0.2)	11 (1)	1730 (25)
G5	39 (3)	29 (3)	6.7 (0.2)	1 (0)	2199 (6)

[a] Average concentrations of three LA-ICP-MS data in each sample are shown with the standard deviation (ppma) in parentheses.

The presence of polysynthetic twinning and linear tubes or dotted lines in samples (figures 14 and 15) other than the deep blue sapphire indicates a possible high-pressure geological event that affected the corundum crystals during or after their crystallization. These inclusion combinations in light blue sapphire as well as red group samples might lead to an association with metamorphic sapphire at first glance with the microscope.

Zircon inclusions appeared only in deep blue sapphires and exhibited magmatic features (detailed chemical composition and morphology information will be presented in a forthcoming paper by the authors). The hexagonal color banding in deep blue sapphire is also reminiscent of magmatic sapphire (e.g., Cambodian and Ethiopian; Palke et al., 2019a).

Chemical Features. Various discrimination diagrams of trace element concentrations and ratios have been used to distinguish corundum from different geographic localities (e.g., Sutherland et al., 1998; Zaw et al., 2006; Abduriyim and Kitawaki, 2006; Peucat et al., 2007; Sutherland and Abduriyim, 2009; Zwaan et al., 2015). To explore the similarities and differences between Muling sapphire and material from other deposits, chemical data are plotted with these diagrams against sapphire datasets from around the world. Recognizing the distinct differences in proportions of trace elements in the different color groups, discussions on blue samples and red samples (including pink to purple sapphire) are documented separately below.

Blue Samples. The Ga/Mg ratio vs. Fe diagram and the Fe-Mg-Ti diagram proposed by Peucat et al. (2007) have been applied to geological typing of various sapphire deposits (Schwarz et al., 2008; Zwaan et al., 2015).

In the diagram of Ga/Mg ratio vs. Fe (figure 25), 13 light blue sapphires plot in a relatively restricted area, showing overlap with Yogo Gulch sapphire from Montana and metamorphic (and metasomatic) sapphire. Considering their high iron content (3170–9130 ppmw), the likelihood of a typical metamorphic origin (such as Sri Lanka) is rather low. The Ga/Mg ratio is 0.2–1.5. The 20 deep blue sapphires tend to be much more dispersed in between the fields of magmatic and metamorphic sapphire, with the

TABLE 8. Inclusion type and frequency in different color groups of gem corundum from Muling, China.

Color group	Red[a]	Light blue	Deep blue	Yellow	Green
Number of samples	112	72	88	23	16
Rutile needles	74%	75%	77%	—	31%
Zircon	—	—	9%	—	—
Feldspar	—	17%	—	—	—
Garnet	2%	—	—	4%	—
Twinning	100%	100%	—	100%	100%
Linear/tubes	52%	75%	—	91%	—
Color zoning	—	—	85%	—	—

[a] The red group includes pink, orangy pink, purple, and purplish red.

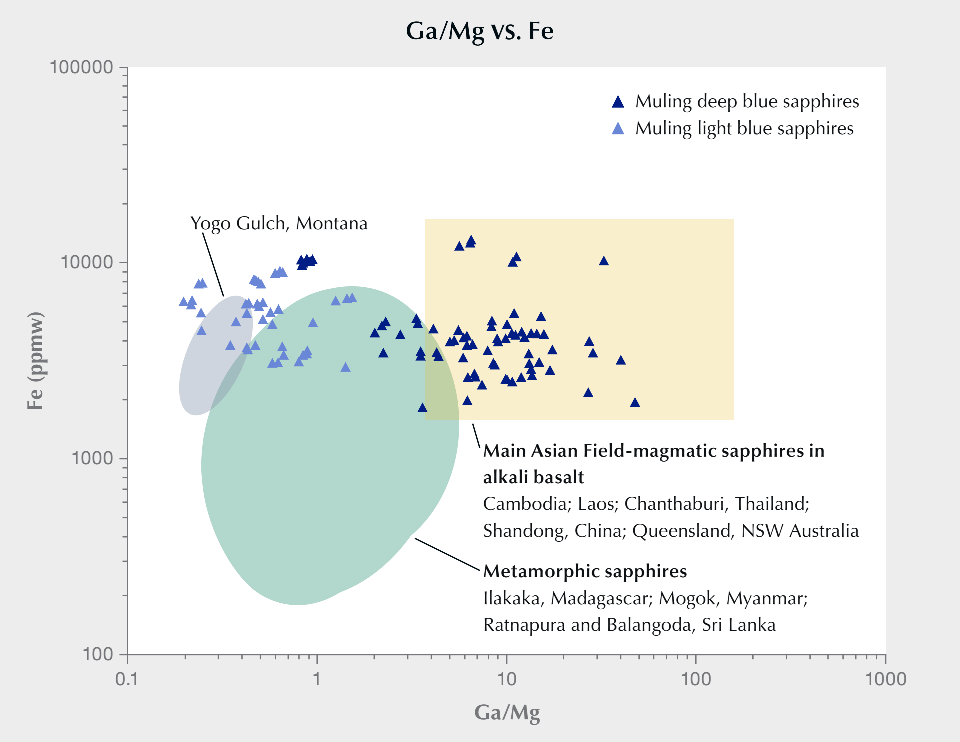

Figure 25. Comparison of Ga/Mg ratio vs. Fe between Muling blue sapphire and metamorphic, magmatic, and Yogo Gulch (Montana) blue sapphire, modified after Peucat et al. (2007) and Zwaan et al. (2015). The 13 Muling light blue sapphires overlap with metamorphic and Yogo sapphires at their higher level of Fe concentration. The 20 Muling deep blue sapphires are plotted in the fields of both magmatic and metamorphic sapphire. Note that both horizontal and vertical axes are displayed in log units rather than linear coordinates to display the data distribution in a more compact form.

Ga/Mg ratio varying from 0.8 to 47 and iron content of 1834–13162 ppmw. In the Fe-Mg-Ti diagram (figure 26), the chemical fingerprint of Muling light blue and deep blue sapphire exhibits a consistent trend

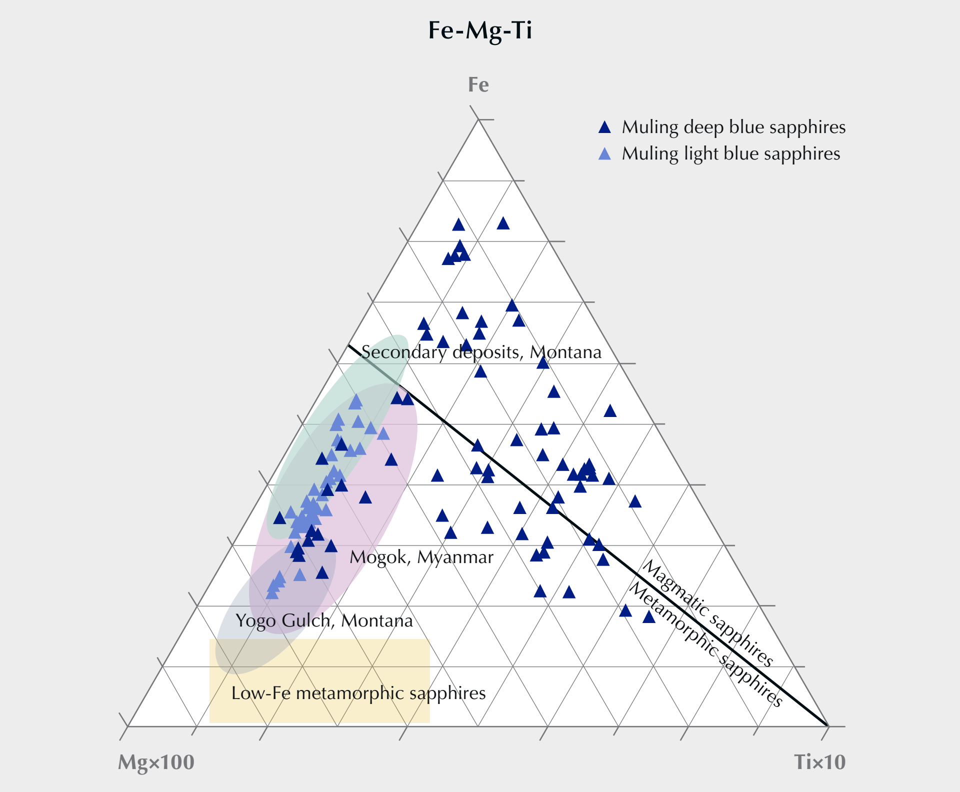

Figure 26. Fe-Mg-Ti diagram, modified after those of Peucat et al. (2007) and Zwaan et al. (2015), plotted in ppmw. The gray area indicates Yogo sapphire, while the green area refers to sapphire from secondary deposits elsewhere in Montana. Sapphire from Mogok exhibits a distribution typical of metamorphic origins (pink area). The yellow rectangle indicates classic metamorphic sapphire with low iron content.

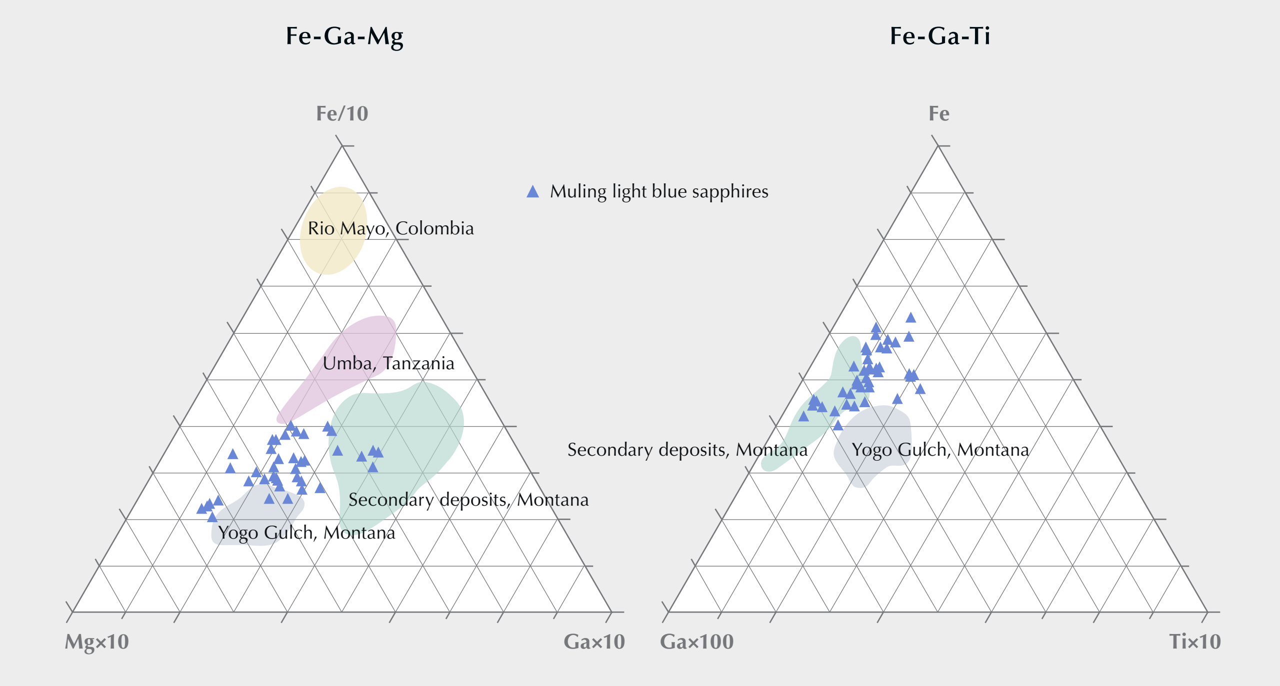

Figure 27. Left: The Fe-Ga-Mg diagram to separate Muling light blue sapphire from Montana secondary deposit sapphire, modified after Peucat et al. (2007) and Zwaan et al. (2015), plotted in ppmw. Right: The Fe-Ga-Ti diagram to distinguish Muling light blue sapphire from Montana Yogo sapphire. Data for Montana sapphire from Renfro et al. (2018).

from the Ga/Mg ratio vs. Fe diagram: Light blue sapphire falls into the area of metamorphic sapphire (e.g., Mogok, Myanmar) and Yogo Gulch (Montana) sapphire along the iron-magnesium axis, while the deep blue sapphire is distributed in both magmatic and metamorphic areas. Since Muling's light blue sapphire exhibits similarities with Montana sapphire (figures 25 and 26), two additional mathematical models are applied for further separation (figure 27). In an Fe-Ga-Mg diagram, Muling samples can be distinguished partially from Montana sapphire—from both secondary deposits and the primary deposit at Yogo Gulch. And in an Fe-Ga-Ti diagram, Muling sapphire shows a somewhat different distribution from that of Yogo sapphire.

Red Group Samples (Pink, Orangy Pink, Purple, and Purplish Red). Binary and ternary plots of the significant trace elements chromium, titanium, iron, and gallium are the most widely used discriminants for geological formation environments (Garnier et al., 2002; Rankin et al., 2003; Schwarz et al., 2008). In the plot of Fe_2O_3 vs. Cr_2O_3 proposed by Schwarz et al. (2008) to distinguish geological types, chemical fingerprints of Muling red group samples are mainly distributed in the field of magmatic-related ruby, with high iron contents (figure 28). This plot also shows that the 31 red, pink, and purple samples overlap with ruby from Winza, Tanzania. A few spots with higher chromium content overlap with Malawi ruby. Most of the analyzed samples in this group consisted of pink sapphire; only a limited number of highly saturated red samples were collected and analyzed due to their rarity in the surveyed locations. Thus, in general, the chromium levels for the entire group of Muling red samples appear low.

Geological Origins of Muling Sapphire. Over the past 30 years, corundum specimens from the Muling area have only been found in alluvial sediments, and the ultimate source rocks have not yet been located. The crystallization conditions for corundum are much too difficult to ascertain for these secondary deposits (Giuliani et al., 2014).

Although the source rock of Muling sapphire needs further exploration, the internal features and the spectral and chemical analyses in this study provide some hints to their origin. The study of syngenetic and protogenetic inclusions makes it possible to extract valuable information about the growth environment. Zircon inclusions in the deep blue samples can provide age information on Muling sapphire (related information will be published in a forthcoming paper by the authors). Rounded anorthite inclusions in light blue sapphire revealed a higher formation temperature for the inclusion compared to the ideal crystallization point. The multiphase inclusion in a red group sample with daughter minerals (figure 13) indicated crystallization from a saturated liquid after it was trapped. And chemical compositions of sillimanite and anorthite (daughter minerals) reflected a sample of the fluid in which the host crystal grew (Roedder, 1962).

The UV-Vis-NIR spectra of the two types of deep blue sapphire display the diversity of the formation history of Muling sapphire. By observing the presence or absence of the absorption band (related to the basaltic environment; Smith, 1978) in the near-infrared range centered around 880 nm of the UV-Vis-NIR spectra (figures 22 and 23), it is possible to quickly distinguish between two sapphires of different geological origins, even though they might be very similar in appearance and have been discovered from the same deposit.

As for chemical characteristics, the plots in figures 25–28 provide some information related to the growth environment of Muling sapphire. The light blue sapphire material exhibits atypical metamorphic features with high iron concentrations. The deep blue sapphire material is distributed in the fields of both magmatic and metamorphic sapphire. However, these trace element diagrams should be used with caution since the corundum coloration may strongly influence the results of the discrimination (Wong et al., 2017; Sorokina et al., 2019), which may conflict with other evidence in deciphering the geological origin (Palke et al., 2018). Therefore, the FeO-Cr_2O_3-MgO-V_2O_3 vs. FeO + TiO_2 + Ga_2O_3 chemical classification diagram proposed by Giuliani et al. (2015) is applied for light blue and deep blue sapphire in figure 29 and for pink and purple sapphire in figure 30. As shown in figure 29, most of the light blue sapphire is confined within the "metasomatic corundum" field, while few spots lie in the typical magmatic field. The deep blue sapphire is divided into two parts. One part lies in the "metasomatic corundum" field. Other deep blue sapphire lies in the overlapping area of the "sapphire in alkali basalts" field and the "sapphire in alkali basalts" field. Considering the overall geological background and the information on zircon inclusions, deep blue sapphire showed a closer relationship with basalts. The red group samples lie mainly in the "metasomatic" field in this plot (figure 26), similar to the result for light blue sapphire. Only a few spots lie in the "ruby in mafic-ultramafics" field. Thus, the FeO-Cr_2O_3-MgO-V_2O_3 vs. FeO + TiO_2 + Ga_2O_3 diagram suggests the possibility of a metasomatic origin for Muling light blue sapphires and red group samples.

However, there are still some uncertainties about the origins of geological formation conditions. The deep blue sapphire material exhibits two types of UV-

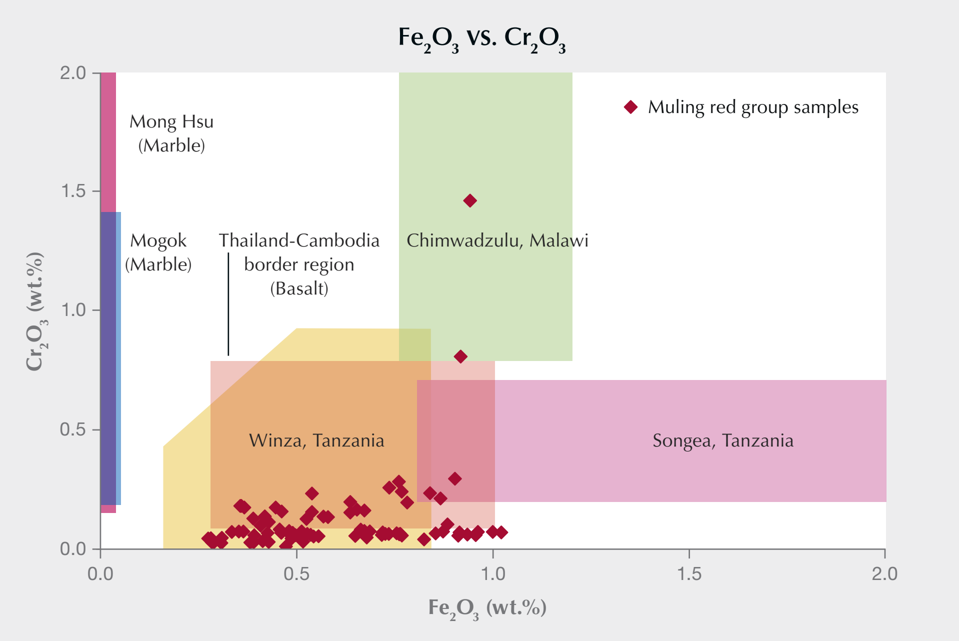

Figure 28. A binary plot of Fe_2O_3 vs. Cr_2O_3, modified after Schwarz et al. (2008). The chemical distribution of the 31 reddish samples from Muling overlaps mainly with magmatic ruby from Thailand and Tanzania.

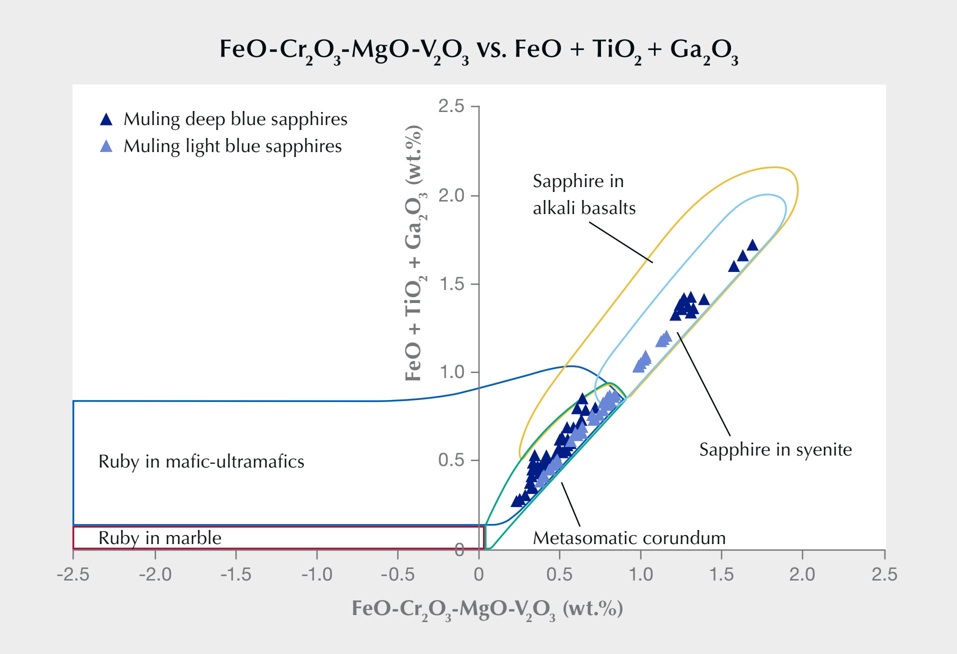

Figure 29. Trace element chemistry plot of FeO-Cr$_2$O$_3$-MgO-V$_2$O$_3$ vs. FeO + TiO$_2$ + Ga$_2$O$_3$ for Muling light blue and deep blue sapphire. Modified after Giuliani et al. (2015).

Vis spectra with distinctly different features in the near-infrared range (see figures 22 and 23), which reveal different growth environments. Angular color zoning has never been observed in red, light blue, and yellow samples but is common in deep blue samples, also indicating different formation environments. Therefore, additional study is needed to explore the true origin of Muling sapphire.

CONCLUSIONS

This study presented a comprehensive set of gemological data on a deposit of fine-quality sapphire beneath the fertile soils of northeastern China. Gemological characteristics including color, clarity, and carat weight indicate the quality of Muling sapphire. The samples showed a full range of hues and saturations, and clarity ranged from transparent to

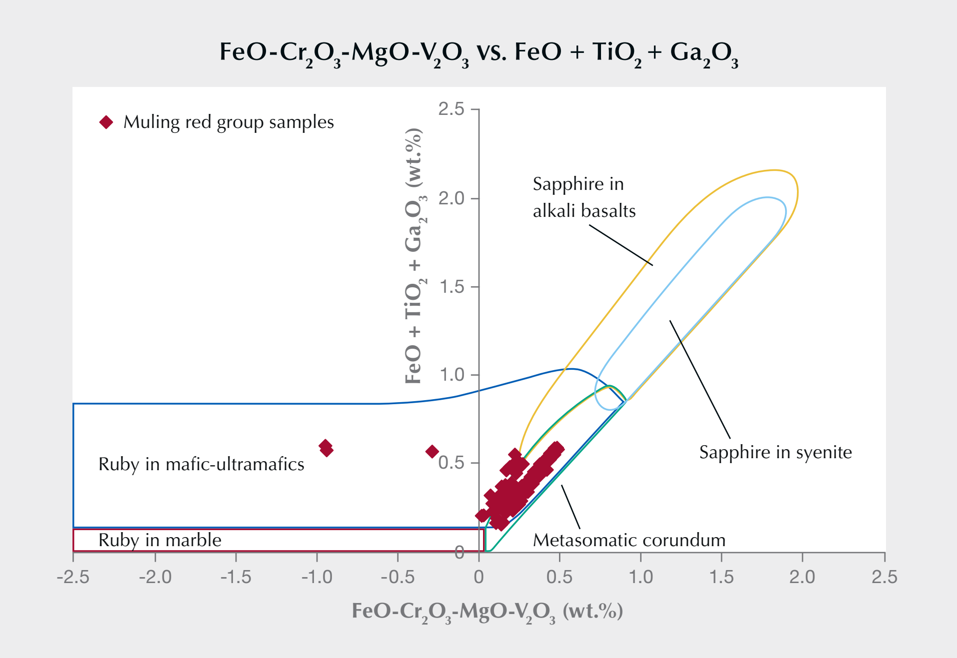

Figure 30. Chemical distribution plot of FeO-Cr$_2$O$_3$-MgO-V$_2$O$_3$ vs. FeO + TiO$_2$ + Ga$_2$O$_3$ for red group samples from Muling. Modified after Giuliani et al. (2015).

semitransparent. Most samples weighed 1–3 ct, with the largest rough sample reaching 51 ct. Microscopic observation revealed rutile needles, tubes, hexagonal zoning, and twinning, along with mineral inclusions (such as anorthite and zircon) as typical internal features in Muling sapphire.

Quantitative analyses with spectroscopy and trace element chemistry determined correlations between chromophore mechanisms and trace elements for each color group of samples. The spectra of blue sapphire material also indicated a mixture of geological formation environments, which were evidenced by their different appearances. Analyses of chemical data utilizing multiple discrimination models further demonstrated that Muling has a more diverse geological environment than typical magmatic or metamorphic settings. Deep blue samples showed dispersed chemical fingerprints across magmatic and metamorphic sapphire. Light blue samples were more consistent with chemical compositions of metamorphic (or metasomatic) sapphire. Red group samples mainly showed metasomatic features with high iron contents. Muling sapphire, known for being of predominantly basaltic origin, produced wide color varieties from a rather limited geographic area. This deposit is a rare example that is distinctly different from common alkali basaltic deposits (e.g., Australia or Shandong, China).

The study of Muling sapphire enriched our knowledge of basalt-related gem corundum with various gemological and geological characteristics. The geological formation origin of Muling sapphire is a subject that deserves further study, and the exploration of their aesthetic qualities will continue as well.

ABOUT THE AUTHORS
Ms. Liu (yim2015@163.com) is a PhD student, and Dr. Lu (renlu.cc@gmail.com) is a distinguished professor, at the Gemmological Institute, China University of Geosciences in Wuhan.

ACKNOWLEDGMENTS
The authors would like to thank the reviewers and editors for their thoughtful suggestions that substantially improved this manuscript. We especially thank Aijun Yi for his help on the field trips and sample collection. We also express our gratitude to lifelong friend Leiguang Zheng for his enthusiastic support on our field trips and his telling of the region’s history and natural heritage.

REFERENCES

Abduriyim A., Kitawaki H. (2006) Determination of the origin of blue sapphire using laser ablation inductively coupled plasma mass spectrometry (LA-ICP-MS). *Journal of Gemmology*, Vol. 30, No. 1-2, pp. 23–36.

Beran A., Rossman G.R. (2006) OH in naturally occurring corundum. *European Journal of Mineralogy*, Vol. 18, No. 4, pp. 441–447, http://dx.doi.org/10.1127/0935-1221/2006/0018-0441

Chen T., Ai H., Yang M., Zheng S., Liu A.Y. (2011) Brownish red zircon from Muling, China. *G&G*, Vol. 47, No. 1, pp. 36–41, http://dx.doi.org/10.5741/GEMS.47.1.36

Chen T., Liu Y., Yin Z., Liu N. (2013) Gemology and spectra characterization of gem garnet from Muling City, Heilongjiang Province. *Spectroscopy and Spectral Analysis*, Vol. 33, No. 11, pp. 2964–2967, http://dx.doi.org/10.3964/j.issn.1000-0593(2013)11-2964-04 [in Chinese].

Cheng Y., Wang J., Tian L.G., Zhang H., Li J. (2009) Application of ion implantation technique in optimization treatment of Shandong sapphire. *Journal of Synthetic Crystals*, Vol. 38, No. 6, pp. 1472–1476. Chinese with English abstract, http://dx.doi.org/10.16553/j.cnki.issn1000-985x.2009.06.002 [in Chinese].

Dubinsky E.V., Stone-Sundberg J., Emmett J.L. (2020) A quantitative description of the causes of color in corundum. *G&G*, Vol. 56, No. 1, pp. 2–28, http://dx.doi.org/10.5741/GEMS.56.1.2

Editorial Committee of Muling (1989) *The County Chronicle of Muling*. Chinese Cultural and Historical Press, Beijing, 11 pp.

Emmett J.L., Douthit T.R. (1993) Heat treating the sapphires of Rock Creek, Montana. *G&G*, Vol. 29, No. 4, pp. 250–272, http://dx.doi.org/10.5741/GEMS.29.4.250

Emmett J.L., Scarratt K., McClure S.F., Moses T., Douthit T.R., Hughes R., Novak S., Shigley J.E., Wang W., Bordelon O., Kane R.E. (2003) Beryllium diffusion of ruby and sapphire. *G&G*, Vol. 39, No. 2, pp. 84–135, http://dx.doi.org/10.5741/GEMS.39.2.84

Emmett J.L., Stone-Sundberg J.L., Guan Y., Sun Z. (2017) The role of silicon in the color of gem corundum. *G&G*, Vol. 53, No. 1, pp. 42–47, http://dx.doi.org/10.5741/GEMS.53.1.42

Emori K., Kitawaki H., Okano M. (2014) Beryllium-diffused corundum in the Japanese market, and assessing the natural vs. diffused origin of beryllium in sapphire. *Journal of Gemmology*, Vol. 34, No. 2, pp. 130–137.

Feng Z.-Q., Liu Y.-J., Li L., Jin W., Jiang L.-W., Li W.-M., Wen Q.-B., Zhao Y.-L. (2019) Geochemical and geochronological constraints on the tectonic setting of the Xinlin ophiolite, northern Great Xing’an Range, NE China. *Lithos*, Vol. 326-327, pp. 213–229, http://dx.doi.org/10.1016/j.lithos.2018.12.018

Ferguson J., Fielding P.E. (1971) The origins of the colours of yellow, green and blue sapphires. *Chemical Physics Letters*, Vol. 10, No. 3, pp. 262–265, http://dx.doi.org/10.1016/0009-2614(71)80282-8

——— (1972) The origins of the colors of natural yellow, blue, and green sapphires. *Australian Journal of Chemistry*, Vol. 25, No. 7, pp. 1371–1385, http://dx.doi.org/10.1071/ch9721371

Galibert O., Hughes R.W. (1995) Chinese ruby and sapphire - a brief history. *Journal of Gemmology*, Vol. 24, No. 7, pp. 467–473.

Giuliani G., Ohnenstetter D., Fallick A.E., Groat L.A., Fagan A.J. (2014) The geology and genesis of gem corundum deposits. In L.A. Groat, Ed., *Geology of Gem Deposits*, Mineralogical Association of Canada (MAC), pp. 29–112.

Giuliani G., Pivin M., Fallick A.E., Ohnenstetter D., Song Y., Demaiffe D. (2015) Geochemical and oxygen isotope signatures of mantle corundum megacrysts from the Mbuji-Mayi kimberlite, Democratic Republic of Congo, and the Changle alkali basalt, China. *Comptes Rendus Geoscience*, Vol. 347, No. 1, pp. 24–34, http://dx.doi.org/10.1016/j.crte.2014.12.003

Gu Z., Xie Y., Gao Y., Ren X., Cheng C., Wang S. (2018) Quantitative assessment of soil productivity and predicted impacts of water erosion in the black soil region of northeastern China. *Science of the Total Environment*, Vol. 637-638, pp. 706–716. http://dx.doi.org/10.1016/j.scitotenv.2018.05.061

Gübelin E.J., Koivula J.I. (1986) *Photoatlas of Inclusions in Gemstones*. Opinio Verlag, Basel, Switzerland.

Guo J., Wang F., Yakoumelos G. (1992) Sapphires from Changle in Shandong Province, China. *G&G*, Vol. 28, No. 4, pp. 255–260, http://dx.doi.org/10.5741/GEMS.28.4.255

Hänni H.A. (1994) Origin determination for gemstones: Possibilities, restrictions, and reliability. *Journal of Gemmology*, Vol. 24, No. 3, pp. 139–148.

Hsu T., Lucas A., Kane R.E., McClure S.F., Renfro N.D. (2017) Big Sky country sapphire: Visiting Montana's alluvial deposits. *G&G*, Vol. 53, No. 2, pp. 215–227, http://dx.doi.org/10.5741/GEMS.53.2.215

Hu L., Pan S., Lu R., Zheng J., Dai H., Guo A., Yu L., Sun H. (2022) Origin of gem-quality megacrysts in the Cenozoic alkali basalts from the Muling area, northeastern China. *Lithos*, Vol. 422–423, article no. 106720, http://dx.doi.org/10.1016/j.lithos.2022.106720

Huang W., Ni P., Shui T., Pan J., Fan M., Yang Y., Chi Z., Ding J. (2021) Trace element geochemistry and mineral inclusions constraints on the petrogenesis of a marble-hosted ruby deposit in Yunnan Province, China. *Canadian Mineralogist*, Vol. 59, No. 2, pp. 381–408, http://dx.doi.org/10.3749/canmin.2000054

Jochum K.P., Nohl U., Herwig K., Lammel E., Stoll B., Hofmann A.W. (2005) GeoReM: a new geochemical database for reference materials and isotopic standards. *Geostandards and Geoanalytical Research*, Vol. 29, No. 3, pp. 333–338, http://dx.doi.org/10.1111/j.1751-908x.2005.tb00904.x

Keller A.S., Keller P.C. (1986) The sapphires of Mingxi, Fujian Province, China. *G&G*, Vol. 22, No. 1, pp. 41–45, http://dx.doi.org/10.5741/GEMS.22.1.41

Keller P.C., Wang F. (1986) A survey of the gemstone resources of China. *G&G*, Vol. 22, No. 1, pp. 3–13, http://dx.doi.org/10.5741/GEMS.22.1.3

Koivula J.I., Fryer C.W. (1987) Sapphirine (not sapphire) in a ruby from Bo Rai, Thailand. *Journal of Gemmology*, Vol. 20, No. 6, pp. 369–370.

Lafuente B., Downs R.T., Yang H., Stone N. (2015) 1. The power of databases: The RRUFF project. In T. Armbruster and R.M. Danisi, Eds., *Highlights in Mineralogical Crystallography*. De Gruyter, Berlin, pp. 1–30.

Lannes B., Zhang C. (2020) China's unstoppable 2020 luxury market. Bain & Company, December 16, https://www.bain.com/insights/chinas-unstoppable-2020-luxury-market/

Li Y., Xu W.-L., Zhu R.-X., Wang F., Ge W.-C., Sorokin A.A. (2020) Late Jurassic to early Cretaceous tectonic nature on the NE Asian continental margin: Constraints from Mesozoic accretionary complexes. *Earth-Science Reviews*, Vol. 200, article no. 103042, http://dx.doi.org/10.1016/j.earscirev.2019.103042

Ling Y.-Y., Zhang J.-J., Liu K., Ge M.-H., Wang M., Wang J.-M. (2017) Geochemistry, geochronology, and tectonic setting of Early Cretaceous volcanic rocks in the northern segment of the Tan–Lu Fault region, northeast China. *Journal of Asian Earth Sciences*, Vol. 144, pp. 303–322, http://dx.doi.org/10.1016/j.jseaes.2016.12.025

Liu Y., Lu R. (2016) Gem News International: Ruby and sapphire from Muling, China. *G&G*, Vol. 52, No. 1, pp. 98–100.

Liu Y., Hu Z., Gao S., Günther D., Xu J., Gao C., Chen H. (2008) In situ analysis of major and trace elements of anhydrous minerals by LA-ICP-MS without applying an internal standard. *Chemical Geology*, Vol. 257, No. 1-2, pp. 34–43, http://dx.doi.org/10.1016/j.chemgeo.2008.08.004

Lu R. (2012) Color origin of lavender jadeite: An alternative approach. *G&G*, Vol. 48, No. 4, pp. 273–283.

Lu R., Shen A.H. (2011) Lab Notes: Unusually high beryllium in three blue sapphires. *G&G*, Vol. 47, No. 3, pp. 232–233.

Miquelle D., Darman Y., Seryodkin I. (2011) *Panthera tigris* ssp. *Altaica*. The IUCN Red List of Threatened Species, https://www.iucnredlist.org

Palke A.C., Breeding C.M. (2017) The origin of needle-like rutile inclusions in natural gem corundum: A combined EPMA, LA-ICP-MS, and nanoSIMS investigation. *American Mineralogist*, Vol. 102, No. 7, pp. 1451–1461.

Palke A.C., Wong J., Verdel C., Ávila J.N. (2018) A common origin for Thai/Cambodian rubies and blue and violet sapphires from Yogo Gulch, Montana, USA? *American Mineralogist*, Vol. 103, No. 3, pp. 469–479.

Palke A.C., Saeseaw S., Renfro N.D., Sun Z., McClure S.F. (2019a) Geographic origin determination of blue sapphire. *G&G*, Vol. 55, No. 4, pp. 536–579, http://dx.doi.org/10.5741/GEMS.55.4.536

——— (2019b) Geographic origin determination of ruby. *G&G*, Vol. 55, No. 4, pp. 580–613, http://dx.doi.org/10.5741/GEMS.55.4.580

Pan S., Zheng J., Griffin W.L., Xu Y., Li X. (2015) Nature and evolution of the lithospheric mantle beneath the eastern Central Asian Orogenic Belt: Constraints from peridotite xenoliths in the central part of the Great Xing'an Range, NE China. *Lithos*, Vol. 238, pp. 52–63, http://dx.doi.org/10.1016/j.lithos.2015.09.013

Pardieu V. (2013) Blue sapphires and Beryllium: An unfinished world quest. *InColor*, Vol. 23, pp. 36–43.

Peucat J.J., Ruffault P., Fritsch E., Bouhnik-Le Coz M., Simonet C., Lasnier B. (2007) Ga/Mg ratio as a new geochemical tool to differentiate magmatic from metamorphic blue sapphires. *Lithos*, Vol. 98, No. 1-4, pp. 261–274, http://dx.doi.org/10.1016/j.lithos.2007.05.001

Powell R.C. (1998) *Physics of Solid-State Laser Materials*. Springer-Verlag, New York, 423 pp.

Qiu Z., Yang J., Yang Y., Yang S., Li C., Wang Y., Lin W., Yang X. (2007) Trace element and hafnium isotopes of Cenozoic basalt-related zircon megacrysts at Muling, Heilongjiang province, northeast China. *Acta Petrologica Sinica*, Vol. 23, No. 2, pp. 481–492. Chinese with English abstract, http://dx.doi.org/10.3969/j.issn.1000-0569.2007.02.024

Rankin A.H., Greenwood J., Hargreaves D. (2003) Chemical fingerprinting of some East African gem rubies by laser ablation ICP-MS. *Journal of Gemmology*, Vol. 28, No. 8, pp. 473–482.

Renfro N.D., Palke A.C., Berg R.B. (2018) Gemological characterization of sapphires from Yogo Gulch, Montana. *G&G*, Vol. 54, No. 2, pp. 184–201, http://dx.doi.org/10.5741/GEMS.54.2.184

Roedder E. (1962) Ancient fluids in crystals. *Scientific American*, Vol. 207, No. 4, pp. 38–47, http://dx.doi.org/10.1038/scientificamerican1062-38

Schmetzer K., Bank H. (1981) The colour of natural corundum. *Neues Jahrbuch Fur Mineralogie-Monatshefte*, Vol. 11, No. 2, pp. 59–68.

Schwarz D., Pardieu V., Saul J.M., Schmetzer K., Laurs B.M., Giuliani G., Klemm L., Malsy A.-K., Erel E., Hauzenberger C., Du Toit G., Fallick A.E., Ohnenstetter D. (2008) Rubies and sapphires from Winza, central Tanzania. *G&G*, Vol. 44, No. 4, pp. 322–347, http://dx.doi.org/10.5741/GEMS.44.4.322

Smith G. (1978) Evidence for absorption by exchange-coupled Fe^{2+}-Fe^{3+} pairs in the near infra-red spectra of minerals. *Physics and Chemistry of Minerals*, Vol. 3, No. 4, pp. 375–383, http://dx.doi.org/10.1007/bf00311848

Sorokin A., Owens P., Láng V., Jiang Z.-D., Michéli E., Krasilnikov P. (2021) "Black soils" in the Russian soil classification system, the US Soil Taxonomy and the WRB: Quantitative correlation and implications for pedodiversity assessment. *CATENA*, No. 196, pp. 104824, http://dx.doi.org/10.1016/j.catena.2020.104824

Sorokina E.S., Rassomakhin M.A., Nikandrov S.N., Karampelas S., Kononkova N.N., Nikolaev A.G., Anosova M.O., Somsikova A.V., Kostitsyn Y.A., Kotlyarov V.A. (2019) Origin of blue sapphire in newly discovered spinel–chlorite–muscovite rocks within meta-ultramafites of Ilmen Mountains, South Urals of Russia: Evidence from mineralogy, geochemistry, Rb-Sr and Sm-Nd isotopic data. *Minerals*, Vol. 9, No. 1, pp. 36, http://dx.doi.org/10.3390/min9010036

Su L. (1990) Sapphires from east of Heilongjiang Province. *Geology of Building Materials*, No. 2, pp. 11+10. Chinese with English abstract.

Sun J.X. (1995) Basalts related to ruby and sapphire in eastern Heilongjiang and reconstruction of Paleovolcanic mechanism. *Acta Petrologica et Mineralogica*, No. 14, pp. 126–132. Chinese with English abstract.

Sun J.X., Li F., Dang Y.S., Cui G., Zhou Y.B. (2005) Mineralogical features of ruby and sapphire from Heilongjiang Province. *Acta Petrologica et Mineralogica*, Vol. 24, No. 1, pp. 62–66. Chinese with English abstract, http://dx.doi.org/10.3969/j.issn.1000-6524.2005.01.007

Sutherland F.L., Abduriyim A. (2009) Geographic typing of gem corundum: a test case from Australia. *Journal of Gemmology*, Vol. 31, No. 5-8, pp. 203–210.

Sutherland F.L., Hoskin P.W.O., Fanning C.M., Coenraads R.R. (1998) Models of corundum origin from alkali basaltic terrains: a reappraisal. *Contributions to Mineralogy and Petrology*, Vol. 133, No. 4, pp. 356–372, http://dx.doi.org/10.1007/s004100050458

Tatian B. (1984) Fitting refractive-index data with the Sellmeier dispersion formula. *Applied Optics*, Vol. 23, No. 24, pp. 4477–4485, http://dx.doi.org/10.1364/AO.23.004477

Wang C., Yang Y., Li G. (1992) Oxidation treatment of the sapphires from Shandong Province, China. *Journal of Gemmology*, Vol. 23, No. 4, pp. 195–197.

Wang C., Liu J., Zhang H., Ge J., Xi Z., Wang H. (2019) Mineralogical features and petrogenetic significance of the clinopyroxene and hornblende of the Wuhaolai mafic complex in northern North China Craton, Inner Mongolia. *Earth Sciences Research Journal*, Vol. 23, No. 2, pp. 133–146.

Wang F. (1988) The sapphires of Penglai, Hainan Island, China. *G&G*, Vol. 24, No. 3, pp. 155–160, http://dx.doi.org/10.5741/GEMS.24.3.155

Wang X.-K., Qiu S.-W., Song C.-C., Kulakov A., Tashchi S., Myasnikov E. (2001) Cenozoic volcanism and geothermal resources in northeast China. *Chinese Geographical Science*, Vol. 11, No. 2, pp. 150–154, http://dx.doi.org/10.16509/j.georeview.1999.s1.147

Wang Y., Dou L.R. (1997) Formation time and dynamic characteristics of the northern part of the Tan-Lu fault zone in east China. *Seismology and Geology*, Vol. 19, No. 2, pp. 186–194.

Wilhem C., Windley B.F., Stampfli G.M. (2012) The Altaids of Central Asia: A tectonic and evolutionary innovative review. *Earth-Science Reviews*, Vol. 113, No. 3-4, pp. 303–341, http://dx.doi.org/10.1016/j.earscirev.2012.04.001

Wong J., Verdel C., Allen C.M. (2017) Trace-element compositions of sapphire and ruby from the eastern Australian gemstone belt. *Mineralogical Magazine*, Vol. 81. No. 6, pp. 1551–1576, http://dx.doi.org/10.1180/minmag.2017.081.012

Zaw K., Sutherland F.L., Dellapasqua F., Ryan C.G., Yui T.F., Mernagh T.P., Duncan D. (2006) Contrasts in gem corundum characteristics, eastern Australian basaltic fields: trace elements, fluid/melt inclusions and oxygen isotopes. *Mineralogical Magazine*, Vol. 70, No. 6, pp. 669–687, http://dx.doi.org/10.1180/0026461067060356

Zhang J., Zhou C., Hu C. (2003) Mineralization characteristics of gems in Ailaoshan structural belt, Yunnan Province. *Journal of Gems & Gemology*, Vol. 5, No. 3, pp. 27–30. Chinese with English abstract, http://dx.doi.org/10.15964/j.cnki.027jgg.2003.03.010

Zhang Y.Q., Shi W., Dong S.W. (2003) Cenozoic deformation history of the Tancheng-Lujiang fault zone, North China, and dynamic implications. *The Island Arc*, Vol. 12, No. 3, pp. 281–293, http://dx.doi.org/10.1046/j.1440-1738.2003.00395.x

Zhang Z., Ding H., Dong X., Tian Z., Mu H., Li M., Qin S., Niu Z., Zhang N. (2018) The eocene corundum-bearing rocks in the Gangdese arc, south Tibet: Implications for tectonic evolution of the Himalayan orogen. *Geoscience Frontiers*, Vol. 9, No. 5, pp. 1337–1354, http://dx.doi.org/10.1016/j.gsf.2017.12.011

Zwaan J.C., Buter E., Mertz-Kraus R., Kane R.E. (2015) The origin of Montana's alluvial sapphires. *G&G*, Vol. 51, No. 4, pp. 370–391, http://dx.doi.org/10.5741/GEMS.51.4.370